

# Representational Alignment with Chemical Induced Fit for Molecular Relational Learning

Peiliang Zhang<sup>✉</sup>, *Student Member, IEEE*, Jingling Yuan<sup>✉</sup>, *Senior Member, IEEE*, Qing Xie<sup>✉</sup>, Yongjun Zhu<sup>✉</sup>,  
Lin Li<sup>✉</sup>, *Senior Member, IEEE*

**Abstract**—Molecular Relational Learning (MRL) is widely applied in natural sciences to predict relationships between molecular pairs by extracting structural features. The representational similarity between substructure pairs determines the functional compatibility of molecular binding sites. Nevertheless, aligning substructure representations by attention mechanisms lacks guidance from chemical knowledge, resulting in unstable model performance in chemical space (e.g., functional group, scaffold) shifted data. With theoretical justification, we propose the Representational Alignment with Chemical Induced Fit (ReAlignFit) to enhance the stability of MRL. ReAlignFit dynamically aligns substructure representation in MRL by introducing chemical-Induced Fit-based inductive bias. In the induction process, we design the Bias Correction Function based on substructure edge reconstruction to align representations between substructure pairs by simulating chemical conformational changes (dynamic combination of substructures). ReAlignFit further integrates the Subgraph Information Bottleneck during fit process to refine and optimize substructure pairs exhibiting high chemical functional compatibility, leveraging them to generate molecular embeddings. Experimental results on nine datasets demonstrate that ReAlignFit’s outperforms state-of-the-art models in two tasks and significantly enhances model’s stability in both rule-shifted and scaffold-shifted data distributions.

**Index Terms**—Molecular Relational Learning, Representational Alignment, Chemical Induced Fit, Model Stability.

## I. INTRODUCTION

Molecular Relational Learning (MRL) predicts the interaction between molecular pairs by mining features and properties [1], [2]. MRL has garnered significant attention in natural science research due to its applications in new material design and drug discovery [3]–[5]. The molecular

structure representation-based methods have advantages in MRL and demonstrate satisfactory performance in downstream tasks [6]–[8]. Therefore, accurately representing molecular features becomes critical in MRL.

The functional compatibility of binding sites is an essential determinant of molecular relationships [9]–[11]. Recent research primarily quantifies functional compatibility by calculating the similarity between substructure representations, focusing on molecular representational alignment by attention-based inductive bias [11]–[13]. The molecular interaction is regarded as an essential source of inductive bias, which aligns the properties of paired molecules with the representations of the molecular core features by modeling the chemical reactions between the molecules. The core challenge lies in effectively computing inductive bias within molecular relationships. Existing methods have explored molecular-level [14], substructure-level [15], and hybrid strategy alignment [16].

Nevertheless, applying inductive bias-based representational alignment to MRL involves two key considerations: (1) **Guidance from Domain Knowledge**: Molecular feature representations are frequently influenced by domain knowledge in chemistry or biology [11], [17], [18]. Changes in adjacent atoms or scaffolds within the chemical space influence the chemical properties of molecular substructures [19], [20]. Most of the existing representational alignment methods [2], [21], [22] predominantly compute inductive bias using attention mechanisms, resulting in the results reflecting statistical correlations and overlooking other active atoms that may affect the properties of these substructures. (2) **Dynamic Adaptability of Inductive Bias**: The substructures (functional groups within molecules) involved in chemical reactions are closely related to their paired substructures [23]–[25], meaning that substructures involved in different chemical reactions within the same molecule may differ. Structural shifts in functional groups and scaffolds may induce dynamic changes in the importance patterns of substructures in chemical reactions. Static inductive bias based on attention mechanisms [26], [27] tends to concentrate weights on certain substructures with specific features, failing to account for dynamic changes such as the adaptive adjustment of substructures in MRL.

To tackle these challenges, we first theoretically demonstrate that aligning information between core substructure pairs facilitates stable MRL. With theoretical justification, we propose the **Representational Alignment with Chemical Induced Fit** (ReAlignFit) to improve MRL stability. ReAlignFit generates substructure embedding through the GNN encoder. Inspired by Induced Fit theory [9], we design the Dynamic Representational

This work was supported by the National Natural Science Foundation of China (No. 62472332 and No. 62276196), the National Key Research and Development Program of China (2022YFB2404300) and the China Scholarship Council. (*Corresponding author: Jingling Yuan.*)

Peiliang Zhang is with the School of Computer Science and Artificial Intelligence, Wuhan University of Technology, Wuhan, 430070, China and also with the Department of Library and Information Science, Yonsei University, Seoul, 26493, Republic of Korea. (E-mail: cheungbl@ieee.org)

Jingling Yuan is with the School of Computer Science and Artificial Intelligence, Hubei Key Laboratory of Transportation Internet of Things, Wuhan University of Technology, Wuhan, 430070, China. (E-mail: yjl@whut.edu.cn)

Qing Xie and Lin Li are with the School of Computer Science and Artificial Intelligence, Wuhan University of Technology, Wuhan, 430070, China. (E-mail: {felixxq, cathyililin}@whut.edu.cn)

Yongjun Zhu is with the Department of Library and Information Science, Yonsei University, Seoul, 26493, Korea. (E-mail: zhu@yonsei.ac.kr)

This paper was produced by the IEEE Publication Technology Group. They are in Piscataway, NJ.

Manuscript received April 19, 2021; revised August 16, 2021.

tational Alignment Module (DRAM) with substructure edge reconstruction, whose core is the Bias Correction Function (BCF). BCF simulates dynamic conformational changes (i.e., dynamic adjustments among substructures) during Induced Fit by a self-supervised approach. Combined with the Subgraph Information Bottleneck (S-GIB), DRAM aligns core substructure pairs for potential compatibility in chemical function. ReAlignFit integrates domain knowledge while avoiding errors in identifying core substructures and aligning information caused by spurious attention. Ultimately, we train ReAlignFit by synergistically optimizing molecular representational alignment’s confusion loss and task prediction loss. Experimental results demonstrate that ReAlignFit achieves state-of-the-art predictive performance and significantly improves model stability in both rule-shifted and scaffold-shifted data distributions. The main contributions are listed below:

- We propose ReAlignFit, which introduces domain knowledge into representational alignment for stable MRL. To the best of our literature review, it is the first work to explore the dynamic representational alignment of substructures in different chemical reactions.
- With theoretical justification, we provide a formal certification for the loss function design to align representations between substructures by minimizing differences between core substructures.
- Experiments on two tasks in nine real-world datasets and three different data distributions demonstrate that the predictive performance and stability of ReAlignFit outperforms eight state-of-the-art models.

## II. PRELIMINARIES

In this section, we illustrate how the attention mechanism-based inductive bias affects the stability of MRL with specific examples (Section II-A). We formally describe stable MRL (Section II-B) and conduct a theoretical analysis to reveal feasible solutions to improve MRL stability (Section II-C).

### A. Motivating Example

The inherent biases and errors in the inductive bias due to attention mechanisms [28] are critical factors affecting the stability of MRL. In this subsection, we explain in further detail how the error in inductive bias affects the representational alignment between molecular pairs and the stability of MRL with the example in Fig. 1.

We will explain the impact of inductive bias errors on the representational alignment between substructure pairs by considering the dynamic adaptation of the induction bias and the guidance of chemical domain knowledge. (1) **The impact of dynamic adaptability of inductive bias on representational alignment:** The core substructure determines the reaction may change depending on the paired molecule. In Fig. 1(a), when molecule A reacts with B, the reactive substructure in A is  $-\text{COOH}$ , while with C, it is  $-\text{NH}_2$ . The scaffold of molecule B is  $-\text{OH}$ , while that of molecule C is  $\text{C}=\text{O}$ . This variation in scaffolds results in different reactive substructures in molecule A. However, the  $-\text{COOH}$  is slightly more reactive than  $-\text{NH}_2$  in chemical reactions. The data co-occurrence

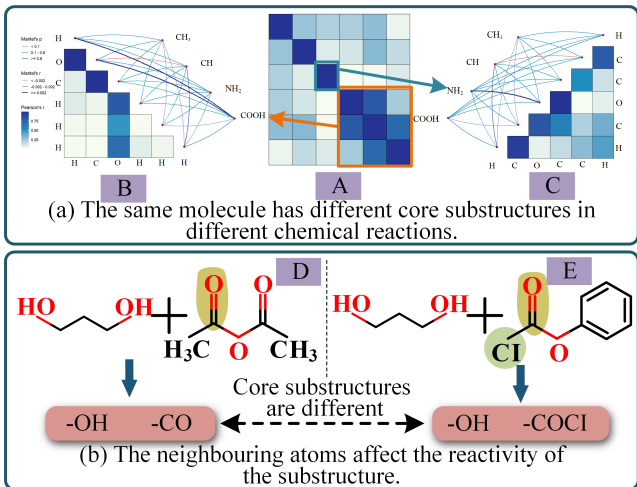


Fig. 1. The motivating example. (a) When molecule A reacts with molecules B and C, the core substructures are  $-\text{COOH}$  and  $-\text{NH}_2$ , respectively. (b) The properties of  $-\text{CO}$  within molecular E are influenced by surrounding reactive atoms  $-\text{Cl}$ , leading to changes in its behavior in chemical reactions.

model of the attentional mechanism causes the inductive bias to overly focus on  $-\text{COOH}$  and ignore the  $-\text{NH}_2$ , which are the true drivers of chemical reactions. This phenomenon indicates that attention-based inductive bias lacks dynamic adaptability to paired molecules in MRL, making it difficult to identify and align the representations of core substructures involved in chemical reactions. (2) **The guidance of domain knowledge on representational alignment:** The properties of molecular substructures are susceptible to influence by surrounding atoms. As shown in Fig. 1(b), the strong electron-adsorption group  $-\text{Cl}$  in molecule E enhances the reactivity of  $-\text{CO}$ . In the esterification reaction, the  $-\text{COCl}$  in molecule E will replace  $-\text{CO}$  and react with the hydroxyl group in alcohols. Inductive bias lacking guidance from domain knowledge usually assigns higher weights to more frequently occurring  $-\text{CO}$ , hindering the alignment of representations for core substructures that drive chemical reactions. Therefore, a key challenge in enhancing the stability is how to dynamically align the representations of core substructures under the guidance of chemical domain knowledge.

### B. Stable Molecular Relational Learning

1) **Molecular Representation and MRL:** We first introduce the problem definitions of molecular representation and MRL in detail. For any molecule  $\mathcal{G}$ , it can be represented as  $\mathcal{G} = (V, \mathcal{E}, \mathcal{X}, A)$ . Here,  $V = \{v_1, v_2, \dots, v_N\}$  denotes the set of nodes.  $\mathcal{E} \in N \times N$  represents the connections between atoms within the molecule, which is closely related to the adjacency matrix  $A$ . If  $(v_i, v_j) \in \mathcal{E}$ , then  $A_{ij} = 1$ ; otherwise,  $A_{ij} = 0$ .  $\mathcal{X} \in \mathbb{R}^{B \times N}$  is the feature matrix, consisting of the atom feature representations. For a given molecular pair  $(\mathcal{G}_x, \mathcal{Y}_{xy}, \mathcal{G}_y)$ , the objective of MRL is to construct a model  $\mathcal{F}_{\text{MRL}} = (\mathcal{F}_{\text{End}}, \mathcal{F}_{\text{Pred}})$  that generates molecular embedding representations  $\mathcal{H}_x$  and  $\mathcal{H}_y$  through the encoder  $\mathcal{F}_{\text{End}}$ , and predicts the relationship  $\mathcal{Y}_{xy}$  between moleculars with the classifier  $\mathcal{F}_{\text{Pred}}$ .

$$\hat{\mathcal{Y}}_{xy} = \mathcal{F}_{\text{MRL}}(\mathcal{G}_x, \mathcal{Y}_{xy}, \mathcal{G}_y) = \mathcal{F}_{\text{Pred}}(\mathcal{F}_{\text{End}}(\mathcal{G}_x, \mathcal{G}_y), \mathcal{Y}_{xy}) \quad (1)$$



2) *Stable MRL*: We further give a detailed definition of Stable MRL based on MRL. Given the dataset  $\mathcal{D} = \{\mathcal{D}_{tra}, \mathcal{D}_{val}, \mathcal{D}_{tes}\}$ ,  $\mathcal{D}_{tra}, \mathcal{D}_{val}, \mathcal{D}_{tes}$  are the training set, validation set, and test set, respectively. In the case of data distribution bias, the data distribution in  $\mathcal{D}_{tra}, \mathcal{D}_{val}, \mathcal{D}_{tes}$  are different from each other. Formally,  $\mathcal{S}(\mathcal{D}_{tra}) \neq \mathcal{S}(\mathcal{D}_{val})$ ,  $\mathcal{S}(\mathcal{D}_{tra}) \neq \mathcal{S}(\mathcal{D}_{tes})$ ,  $\mathcal{S}(\mathcal{D}_{val}) \neq \mathcal{S}(\mathcal{D}_{tes})$ . The specific setup and partitioning of  $\mathcal{D}_{tra}, \mathcal{D}_{val}, \mathcal{D}_{tes}$  will be described in detail in Section IV-A. Stable MRL aims to train a model  $\mathcal{F}_{MRL}^S = (\mathcal{F}_{End}^{tra}, \mathcal{F}_{Pred}^{val}, \mathcal{F}_{Pred}^{tes})$  using  $\mathcal{D}_{tra}$  and  $\mathcal{D}_{val}$  that generalizes well to  $\mathcal{D}_{tes}$ . The model  $\mathcal{F}_{MRL}$  should maintain relatively stable predictive performance in different distribution shifts.

$$\mathcal{F}_{MRL}^S \leftarrow \{\mathcal{F}_{Pred}^{val}(\mathcal{G}_x, \mathcal{Y}_{xy}, \mathcal{G}_y) \simeq \mathcal{F}_{Pred}^{tes}(\mathcal{G}_u, \mathcal{Y}_{uv}, \mathcal{G}_v)\} \quad (2)$$

*s.t.*  $\mathcal{G}_x, \mathcal{G}_y \in \mathcal{D}_{val}, \quad \mathcal{G}_u, \mathcal{G}_v \in \mathcal{D}_{tes}$

Therefore, ReAlignFit aims to learn stable molecular representations consisting of core substructures, thereby improving the model’s predictive performance.

### C. Theoretical Analysis of Stable MRL

Considering that modeling molecular relationships solely from the data perspective easily leads to instability in the model, we introduce the Induced Fit theory in chemistry to identify key factors affecting the stability of MRL at the theoretical analysis stage.

1) *Theoretical Analysis*: The Induced Fit theory describes the dynamic mechanism of specific molecular binding. It emphasizes that matching binding sites (representation similarity between paired substructures) is critical for enhancing binding stability [9], [29]. Inspired by the Induced Fit theory, we attempt to analyze the contribution of matching between substructure pairs to MRL performance stabilization on the theoretical level.

**Theorem II.1.** *Given the molecular pair  $(\mathcal{G}_x, \mathcal{G}_y)$  and the prediction target  $\mathcal{Y}$ , where the substructure  $\mathcal{G}^s$  of  $\mathcal{G}$  consists of core substructure  $\mathcal{G}^c$  and confounding substructure  $\mathcal{G}^n$ . For  $\forall \mathcal{G}_x, \mathcal{G}_y \in \mathcal{G}$ , according to the law of conditional probability,  $\mathcal{P}(\mathcal{G}_x, \mathcal{G}_y; \mathcal{Y}) \geq \mathcal{P}(\mathcal{G}^c; \mathcal{Y} | \mathcal{G}^n)$ . Furthermore, considering the correlation between  $\mathcal{G}^c$  and  $\mathcal{G}^n$ , if there exists a minimal value  $\varepsilon$  such that:*

$$|\mathcal{P}(\mathcal{G}_x, \mathcal{G}_y; \mathcal{Y}) - \mathcal{P}(\mathcal{G}_x^c, \mathcal{G}_y^c; \mathcal{Y}) + \mathcal{P}(\mathcal{G}_x^c; \mathcal{G}_x^n) + \mathcal{P}(\mathcal{G}_y^c; \mathcal{G}_y^n)| \leq \varepsilon \quad (3)$$

where  $\mathcal{P}(\mathcal{G}_x, \mathcal{G}_y; \mathcal{Y})$  is the true probability between molecular pair and the prediction target.  $\mathcal{P}(\mathcal{G}_x^c, \mathcal{G}_y^c; \mathcal{Y})$  is interaction probability between core substructure captured by model learning and prediction target called learning probability.  $\mathcal{P}(\mathcal{G}_x^c; \mathcal{G}_x^n)$  and  $\mathcal{P}(\mathcal{G}_y^c; \mathcal{G}_y^n)$  are the confounding probabilities between core and confounding substructures.

The  $\varepsilon$  measures the similarity between true probability, learning probability, and confounding probability. The discrepancy between true and learned probabilities is derived from the task’s prediction loss, whereas the degree of calibration between substructure representations quantifies the confusion probability. Theorem II.1 demonstrates that when  $\eta$  is sufficiently small, meaning the prediction loss and confusion

probability are small enough, the relationships between molecular pairs can be stably represented. Inspired by Theorem II.1, we optimize model learning by combining prediction loss and confusion probability. This approach guides us in identifying core substructures by substructure representational alignment while reducing the impact of non-core substructures on molecular representations, thereby improving the stability of MRL.

2) *The Proof of Theorem II.1*: Since  $\mathcal{P}(\mathcal{G}_x^n; \mathcal{Y} | \mathcal{G}_x^c)$  is non-negative and  $\mathcal{G}_x^n, \mathcal{G}_y^n$  have little effect on  $\mathcal{Y}$ , according to the law of conditional probability,  $\mathcal{P}(\mathcal{G}_x, \mathcal{G}_y; \mathcal{Y})$  is expressed as:

$$\begin{aligned} \mathcal{P}(\mathcal{G}_x, \mathcal{G}_y; \mathcal{Y}) &= \mathcal{P}(\mathcal{G}_x^c; \mathcal{Y}) + \mathcal{P}(\mathcal{G}_y^n; \mathcal{Y} | \mathcal{G}_x^c, \mathcal{G}_x^n, \mathcal{G}_y^c) \\ &\quad + \mathcal{P}(\mathcal{G}_x^n; \mathcal{Y} | \mathcal{G}_x^c) + \mathcal{P}(\mathcal{G}_y^c; \mathcal{Y} | \mathcal{G}_x^c, \mathcal{G}_x^n, \mathcal{G}_y^n) \quad (4) \\ &\geq \mathcal{P}(\mathcal{G}_x^c; \mathcal{Y}) + \mathcal{P}(\mathcal{G}_y^c; \mathcal{Y} | \mathcal{G}_x^c) \end{aligned}$$

$\mathcal{P}(\mathcal{G}_y^c; \mathcal{Y})$  represents the probability between  $\mathcal{G}_y^c$  and  $\mathcal{Y}$ , which contains at least the conditional probability  $\mathcal{P}(\mathcal{G}_y^c; \mathcal{Y} | \mathcal{G}_x^c)$ . We can obtain  $\mathcal{P}(\mathcal{G}_x, \mathcal{G}_y; \mathcal{Y}) \geq \mathcal{P}(\mathcal{G}^c; \mathcal{Y} | \mathcal{G}^n)$ . According to the properties of conditional probability:

$$\begin{aligned} \mathcal{P}(\mathcal{G}^c; \mathcal{Y} | \mathcal{G}^n) &\approx \mathcal{P}(\mathcal{G}_x^c; \mathcal{Y}) + \mathcal{P}(\mathcal{G}_y^c; \mathcal{Y} | \mathcal{G}_x^c) \\ &:= \mathcal{P}(\mathcal{G}_x^c; \mathcal{Y}) + \mathcal{P}(\mathcal{G}_y^c; \mathcal{Y}) = \mathcal{P}(\mathcal{G}_x^c, \mathcal{G}_y^c; \mathcal{Y}) \quad (5) \end{aligned}$$

Based on Eq (5), and considering that  $\mathcal{P}(\mathcal{G}_x^c; \mathcal{G}_x^n)$  and  $\mathcal{P}(\mathcal{G}_y^c; \mathcal{G}_y^n)$  are non-negative, we have the equation as:

$$\mathcal{P}(\mathcal{G}_x, \mathcal{G}_y; \mathcal{Y}) - \mathcal{P}(\mathcal{G}_x^c, \mathcal{G}_y^c; \mathcal{Y}) + \mathcal{P}(\mathcal{G}_x^c; \mathcal{G}_x^n) + \mathcal{P}(\mathcal{G}_y^c; \mathcal{G}_y^n) \geq 0 \quad (6)$$

Therefore, by increasing  $\mathcal{P}(\mathcal{G}_x^c, \mathcal{G}_y^c; \mathcal{Y})$  and decreasing  $\mathcal{P}(\mathcal{G}_x^c; \mathcal{G}_x^n) + \mathcal{P}(\mathcal{G}_y^c; \mathcal{G}_y^n)$  (i.e., increasing the correlation between the core substructures captured by the model and prediction targets, and decreasing the impact of the confounding substructures on the core substructure representation), we can ensure that there exists a minimal positive number  $\varepsilon$  that satisfies the following relationship:

$$|\mathcal{P}(\mathcal{G}_x, \mathcal{G}_y; \mathcal{Y}) - \mathcal{P}(\mathcal{G}_x^c, \mathcal{G}_y^c; \mathcal{Y}) + \mathcal{P}(\mathcal{G}_x^c; \mathcal{G}_x^n) + \mathcal{P}(\mathcal{G}_y^c; \mathcal{G}_y^n)| \leq \varepsilon \quad (7)$$

## III. METHODOLOGY

Inspired by Theorem II.1, we propose ReAlignFit to enhance the stability of MRL by simulating the dynamic mechanism of molecular binding, as shown in Fig. 2. Based on Substructure Representation-based Interaction Network (SRIN) in Fig. 2(a), we design the Dynamic Representational Alignment Module (DRAM), as shown in Fig. 2(b), which employs BCF and S-GIB to align the core substructure representations (Section III-A). Additionally, we detail the transformation and solution process of Subgraph Information Bottleneck (S-GIB) (Section III-B) and analyze the computational complexity of ReAlignFit (Section III-C).

### A. Representational Alignment with Induced Fit

Induced Fit suggests that chemical reactions between molecules are realized by combining the pre-adaptation of substructures and dynamic adjustments during binding [9]. Guided by it, we design SRIN to simulate the pre-adaptation process. In DRAM, BCF simulates the molecular induction process to align substructure representations, while S-GIB identifies and refines substructures with high chemical functional compatibility.

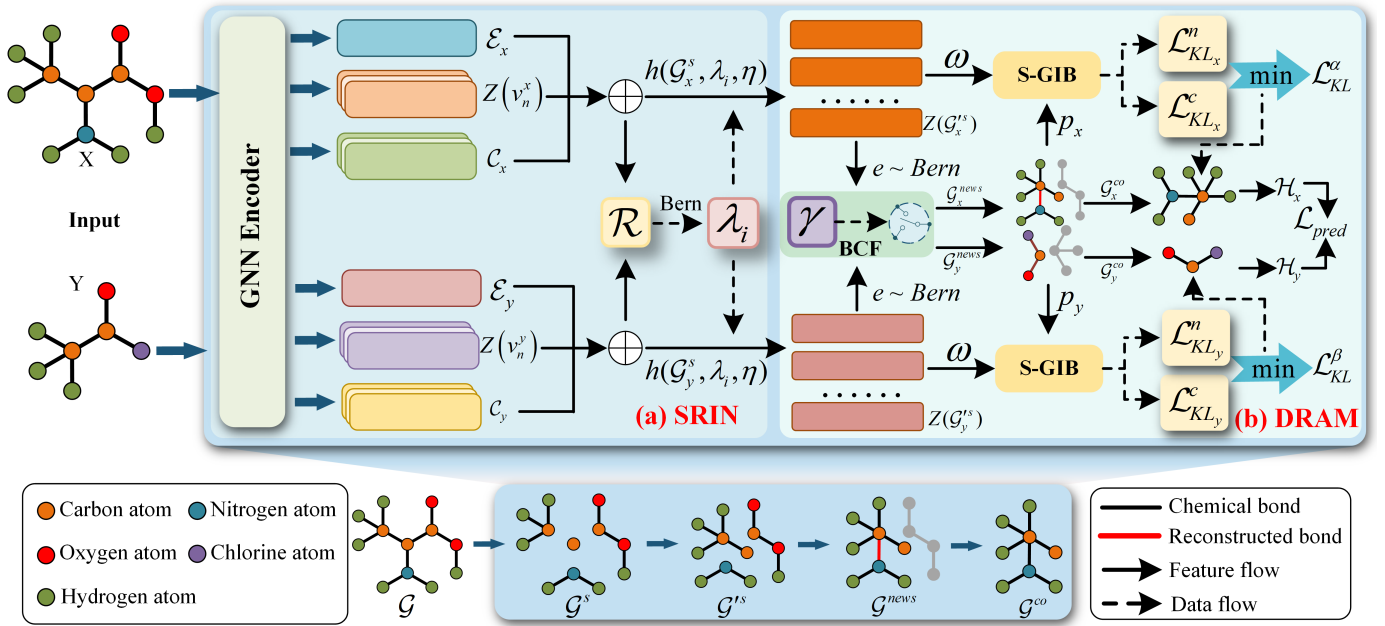


Fig. 2. The model structure of ReAlignFit. (a) SRIN generates substructure representations. (b) DRAM aligns and optimizes the core substructure representations to generate stable representations of molecules.

1) *Substructure Representation-based Interaction Network:* Considering the irregularity of molecular spatial topologies and the effectiveness of GNN in dealing with topological features [8], [30], ReAlignFit utilizes the GNN encoder and an adjacency aggregation strategy to generate embeddings for irregular substructures.

Initially, molecule  $\mathcal{G}$  represented by SMILES [31] are converted into GNN-compatible representations by RDKit [32]. Subsequently, we use neighbourhood feature weighting consisting of adjacency matrix  $\mathcal{E}$ , node feature representation  $\mathcal{Z}(v_n)$ , and neighbourhood structural coefficient  $\mathcal{C}$  as the input for irregular substructure generation. The node feature representation  $\mathcal{Z}^{l+1}(v_n)$  in  $(l+1)$ th layer and neighborhood structural coefficient  $\mathcal{C}$  are defined as follows:

$$\mathcal{Z}^{l+1}(v_n) = \sum_{v_u \in \mathcal{N}(v_n)} (W_u \mathcal{Z}^l(v_u) + W_n \mathcal{Z}^l(v_n))$$

$$\mathcal{C} = \frac{\sigma(\mathcal{Z}(v_n)) \cdot \log \sigma(\mathcal{Z}(v_n))}{\sum_{v_u \in \mathcal{N}(v_n)} \sigma(\mathcal{Z}(v_u)) \cdot \log \sigma(\mathcal{Z}(v_u))} \quad (8)$$

where  $\mathcal{N}(v_n)$  denotes the set of neighbor nodes of node  $v_n$ .  $W$  is the weight matrix and  $\sigma$  is the activation function.  $\mathcal{Z}(\cdot)$  is the embedding representation obtained from the GNN encoder, which can be selected from GIN [33], MPNN [34], GAT [35], or GCN [36]. For molecule  $\mathcal{G}$ , its irregular substructure  $\mathcal{Z}(\mathcal{G}^s)$  is derived by aggregating the central node  $v_n$  and its  $K$ -hop neighbours  $v_n^k$ , weighted by  $\mathcal{C}$ :

$$\mathcal{Z}(\mathcal{G}^s) = \sum_{k=1}^K \sum_{v_u \in v_n^k} (\mathcal{Z}(v_n) || \mathcal{C} \cdot \mathcal{Z}(v_u)) \quad (9)$$

In the subsequent step, we calculate the interaction probability between substructures by Eq (10) to simulate the pre-adaptation process of substructures. We further optimize the molecular substructure representations by noise elimination with Eq (11) results. The substructure interaction probability for pre-adaptation is calculated as follows:

$$\mathcal{R}_i = \sum_{\mathcal{G}_y^{s,j} \in \mathcal{G}_y^s} \sigma(\mathcal{Z}(\mathcal{G}_x^{s,i}), \mathcal{Z}(\mathcal{G}_y^{s,j})) + \frac{1}{J-1} \sum_{\mathcal{G}_y^{s,k} \neq \mathcal{G}_y^{s,j}} \sigma(\mathcal{Z}(\mathcal{G}_x^{s,i}), \mathcal{Z}(\mathcal{G}_y^{s,k})) \quad (10)$$

where  $\sigma(\cdot)$  is a probability function.  $\mathcal{G}_x^{s,i}$  and  $\mathcal{G}_y^{s,j}$  denote the substructures of the paired molecules  $(\mathcal{G}_x, \mathcal{G}_y)$ .  $\mathcal{G}_y^s$  represents the substructure set of molecule  $\mathcal{G}_y$ , containing  $J$  elements. ReAlignFit eliminates unimportant substructures (i.e., those with lower  $\mathcal{R}_i$ ) via the  $\mathcal{R}_i$  and the noise rejection function  $\lambda$  to control the effect of confounding information on substructure representations while generating the optimized substructure representation  $\mathcal{Z}(\mathcal{G}^{ts})$ :

$$\mathcal{Z}(\mathcal{G}^{ts}) = h(\mathcal{G}^s, \lambda_i, \eta) = \lambda_i \mathcal{Z}(\mathcal{G}^{s,i}) + (1 - \lambda_i) \eta$$

$$\lambda_i \sim \text{Bernoulli}(\sigma(\mathcal{R}_i)), \eta \sim (\mu_{\mathcal{Z}(\mathcal{G}^s)}, \sigma_{\mathcal{Z}(\mathcal{G}^s)}^2) \quad (11)$$

where  $\mu_{\mathcal{Z}(\mathcal{G}^s)}$  and  $\sigma_{\mathcal{Z}(\mathcal{G}^s)}^2$  are mean and variance of  $\mathcal{Z}(\mathcal{G}^s)$ , respectively. The refined  $\mathcal{Z}(\mathcal{G}_x^{ts})$  and  $\mathcal{Z}(\mathcal{G}_y^{ts})$  are utilized to dynamic representational alignment.

2) *Dynamic Representational Alignment Module:* Representational alignment methods introducing inductive bias via attention mechanisms rely on static combinations between substructures, ignoring dynamic adjustments in reactions. This limits their ability to capture core substructures driving different chemical reactions. The Induced Fit theory highlights conformational changes of paired substructures, i.e., the dynamic variations of substructure topologies and binding sites during molecular interactions. Therefore, we design the BCF to dynamically adjust substructure binding sites and representational alignment while integrating the S-GIB to identify highly functional compatible substructures (core substructures).

Considering that GNN-based molecular representation methods may ignore the connecting mechanisms of the chemical bonds, we employ a substructure edge reconstruction strategy in DRAM to represent substructure information as accurately as possible. Specifically, we remove the edges between all substructures  $\mathcal{G}^s$  in  $\mathcal{G}$  at the initial stage. DRAM

computes the Bernoulli distribution  $e_{ik}$  between substructures  $\mathcal{G}^{s_i}$  and  $\mathcal{G}^{s_k}$  by edge sampling, and reconstruct the edges with  $e_{ik} = 1$ .  $e_{ik} \sim \text{Bernoulli}(\theta_{ik})$ , where  $\theta_{ik}$  is computed using a Gaussian Kernel function. The new substructure obtained in reconstruction is denoted as  $\mathcal{G}^{news}$ .

After edge reconstruction, we design the Bias Correction Function  $\gamma$  to quantify the degree of alignment between substructures before and after reconstruction. The computation of  $\gamma$  is provided in Eq (22).

$$\gamma = \sum_{j \leq J} \frac{2 \|\sigma(\mathcal{Z}(\mathcal{G}_x^{news}), \mathcal{Z}(\mathcal{G}_y^{s_j}))\|_2^2}{J(\|\sigma(\mathcal{Z}(\mathcal{G}_x^{s_i}), \mathcal{Z}(\mathcal{G}_y^{s_j}))\|_2^2 + \|\sigma(\mathcal{Z}(\mathcal{G}_x^{s_k}), \mathcal{Z}(\mathcal{G}_y^{s_j}))\|_2^2)} \quad (12)$$

where  $\mathcal{G}_x^{news}$  is reconstructed from the substructures  $\mathcal{G}_x^{s_i}$  and  $\mathcal{G}_x^{s_k}$  of molecule  $\mathcal{G}_x$ .  $\mathcal{G}_y^{s_j}$  represents the substructure of molecule  $\mathcal{G}_y$  paired with  $\mathcal{G}_x$ .

In the Induced Fit theory, conformational changes aim to achieve functional compatibility at binding sites, which can be approximately quantified through similarity in vector space [29]. Therefore, we employ cosine similarity to compute the components of  $\gamma$ , quantifying the chemical functional compatibility between substructures.

DRAM dynamically determines whether to perform edge reconstruction and align substructure representation. based on  $\gamma$ . The substructure representation after dynamic adjustment is defined as:

$$\mathcal{G}_x^c = \begin{cases} \text{if } \gamma \geq 1, & \mathcal{G}_x^{news} \\ \text{if } \gamma < 1, & \begin{cases} \text{if } \sigma_{ij} \geq \sigma_{kj}, & \mathcal{G}_x^{s_i} \\ \text{if } \sigma_{ij} < \sigma_{kj}, & \mathcal{G}_x^{s_k} \end{cases} \end{cases} \quad (13)$$

where  $\sigma_{*j} = \|\sigma(\mathcal{Z}(\mathcal{G}_x^{s_*}), \mathcal{Z}(\mathcal{G}_y^{s_j}))\|_2^2$ . The substructure  $\mathcal{G}_y^c$  after dynamic adjustment of  $\mathcal{G}_y$  can be computed similarly.

Considering the advantages of the Graph Information Bottleneck (GIB) in graph optimization and the specific requirements of MRL tasks [5], [15], [37], we further extend the optimization objective of GIB to the subgraph level for core substructure selection and optimization. The refined aim is defined as follows:

**Definition III.1. (S-GIB)** Given a set of graphs and their interaction relationships  $(\mathcal{G}_x, \mathcal{Y}, \mathcal{G}_y)$ ,  $(\mathcal{G}_x^c, \mathcal{G}_y^c)$  and  $(\mathcal{G}_x^n, \mathcal{G}_y^n)$  are the core subgraph pairs and confounding subgraph pairs of  $(\mathcal{G}_x, \mathcal{G}_y)$  and  $\mathcal{Y}$ , respectively. The subgraph  $\mathcal{G}^s = \{\mathcal{G}^c, \mathcal{G}^n\}$ . According to the minimal sufficient principle of mutual information, the optimization objective is defined as:

$$\mathcal{G}^{co} = \text{argmin}(\alpha \mathcal{I}(\mathcal{G}_x^c, \mathcal{G}_y^n) + \beta \mathcal{I}(\mathcal{G}_y^c, \mathcal{G}_x^n) - \mathcal{I}(\mathcal{Y}; \mathcal{G}_x^c, \mathcal{G}_y^c)) \quad (14)$$

$-\mathcal{I}(\mathcal{Y}; \mathcal{G}_x^c, \mathcal{G}_y^c)$  allows the model to fully learn the information of core subgraphs relevant to the prediction target.  $\alpha \mathcal{I}(\mathcal{G}_x^c, \mathcal{G}_y^n) + \beta \mathcal{I}(\mathcal{G}_y^c, \mathcal{G}_x^n)$  minimizes the influence of confounding subgraphs on core subgraphs by eliminating confounding information. The detailed solution process for S-GIB will be presented in Section III-B.

We regard core substructures as core subgraphs in S-GIB and non-core substructures as confounding subgraphs. During the optimization of S-GIB, core substructures representing stable molecular representations are identified, while the influence of other substructures on molecular representations is

minimized. Through the synergy between Eqs (12), (13) and (14), ReAlignFit dynamically selects and aligns the embedded representations of core substructures determining chemical reactions with full consideration of paired molecules.

The core substructure optimized by S-GIB is denoted as  $\mathcal{G}^{co}$ . The final embedding representation  $\mathcal{H}$  is generated by aggregating the core substructures of the molecules.

$$\mathcal{H} = \text{Readout}(\mathcal{Z}(\mathcal{G}^{co1}) || \dots || \mathcal{Z}(\mathcal{G}^{coM})), M \ll N \quad (15)$$

where  $M$  is the number of core substructures.

### B. Model Optimization and S-GIB Solution

We design the loss function  $\mathcal{L}$  with Theorem II.1 and demonstrate the transformation and solution process of S-GIB.

1) *Model Loss Function*: We design the model optimization objective  $\mathcal{L}$  consistent with the derived conclusion in Theorem II.1, which consists of the sum of prediction loss  $\mathcal{L}_{pred}$  and calibration loss  $\mathcal{L}_{KL}$ .

$$\mathcal{L} = \mathcal{L}_{pred} + \alpha \mathcal{L}_{KL}^\alpha + \beta \mathcal{L}_{KL}^\beta \quad (16)$$

where  $\alpha$  and  $\beta$  are hyperparameters that consistent with the settings in Eq (14). To reduce the complexity of mutual information calculation, we transform Eq (14) as follows.

2) *The Upper Bound of  $\alpha \mathcal{I}(\mathcal{G}_x^c, \mathcal{G}_y^n) + \beta \mathcal{I}(\mathcal{G}_y^c, \mathcal{G}_x^n)$  in Eq (14)*: We utilize information-theoretic principles to derive the upper bounds of  $\mathcal{I}(\mathcal{G}_x^c, \mathcal{G}_y^n)$  and  $\mathcal{I}(\mathcal{G}_y^c, \mathcal{G}_x^n)$ , respectively.

**Proposition III.1. (Upper bound of  $\mathcal{I}(\mathcal{G}_x^c, \mathcal{G}_y^n)$ )** Since  $\mathcal{G}_x^c, \mathcal{G}_x^n$  are subgraphs of  $\mathcal{G}_x$ , according to the information transferability of Markov chain, we have

$$\begin{aligned} \mathcal{I}(\mathcal{G}_x^c, \mathcal{G}_y^n) &\leq \min(\mathcal{I}(\mathcal{G}_x^c, \mathcal{G}_x), \mathcal{I}(\mathcal{G}_y^n, \mathcal{G}_x)) \\ &= \min(\iint p(\mathcal{G}_x^c | \mathcal{G}_x, \gamma) \log\left(\frac{p(\mathcal{G}_x^c | \mathcal{G}_x, \gamma)}{p(\mathcal{G}_x^c)}\right) d\mathcal{G}_x^c d\mathcal{G}_x, \\ &\quad \iint p(\mathcal{G}_y^n | \mathcal{G}_x, \gamma) \log\left(\frac{p(\mathcal{G}_y^n | \mathcal{G}_x, \gamma)}{p(\mathcal{G}_y^n)}\right) d\mathcal{G}_y^n d\mathcal{G}_x) \\ &:= \min(KL(p(\mathcal{G}_x^c | \mathcal{G}_x, \gamma) || p(\mathcal{G}_x^c)), \\ &\quad KL(p(\mathcal{G}_y^n | \mathcal{G}_x, \gamma) || p(\mathcal{G}_y^n))) \\ &= \min(\mathcal{L}_{KL_x}^c, \mathcal{L}_{KL_x}^n) \end{aligned} \quad (17)$$

where  $p(\cdot)$  is a posterior distribution function.

Therefore, minimizing  $\mathcal{L}_{KL}^\alpha = \min(\mathcal{L}_{KL_x}^c, \mathcal{L}_{KL_x}^n)$  provides an upper bound for the minimization of  $\mathcal{I}(\mathcal{G}_x^c, \mathcal{G}_y^n)$ . Similarly, the upper bound for minimizing  $\mathcal{I}(\mathcal{G}_y^c, \mathcal{G}_x^n)$  can be obtained by minimizing  $\mathcal{L}_{KL}^\beta = \min(\mathcal{L}_{KL_y}^c, \mathcal{L}_{KL_y}^n)$ .

**The proof of Eq (17).** The  $\mathcal{I}(\mathcal{G}_x^c, \mathcal{G}_y^n)$  is expressed in integral form as:

$$\mathcal{I}(\mathcal{G}_x^c, \mathcal{G}_y^n) = \iint p(\mathcal{G}_x^c, \mathcal{G}_y^n) \log\left(\frac{p(\mathcal{G}_x^c, \mathcal{G}_y^n)}{p(\mathcal{G}_x^c)p(\mathcal{G}_y^n)}\right) d\mathcal{G}_x^c d\mathcal{G}_y^n \quad (18)$$

The probability function  $\gamma$  in Eq (12) is utilized to adjust the conditional probability distribution  $p(\mathcal{G}_x^c, \mathcal{G}_y^n)$ , and  $\mathcal{G}_x^c, \mathcal{G}_y^n$  are conditionally independent of  $\mathcal{G}_x$ . We can obtain  $p(\mathcal{G}_x^c | \mathcal{G}_x) = p(\mathcal{G}_x^c | \mathcal{G}_x, \gamma)$ . Further,  $\mathcal{I}(\mathcal{G}_x^c, \mathcal{G}_y^n)$  is expressed as:

$$\begin{aligned} \mathcal{I}(\mathcal{G}_x^c, \mathcal{G}_y^n) &= \iint p(\mathcal{G}_x^c | \mathcal{G}_x, \gamma) \log\left(\frac{p(\mathcal{G}_x^c | \mathcal{G}_x, \gamma)}{p(\mathcal{G}_x^c)}\right) d\mathcal{G}_x^c d\mathcal{G}_x \\ &:= KL(p(\mathcal{G}_x^c | \mathcal{G}_x, \gamma) || p(\mathcal{G}_x^c)) \\ &= \mathcal{L}_{KL_x}^c \end{aligned} \quad (19)$$



The result of Eq (19) indicates that  $\mathcal{I}(\mathcal{G}_x^c, \mathcal{G}_x)$  can be computed by the KL divergence between  $\mathcal{G}_x^c$  and  $\mathcal{G}_x$ . Similarly,  $\mathcal{I}(\mathcal{G}_x^n, \mathcal{G}_x) = KL(p(\mathcal{G}_x^n|\mathcal{G}_x, \gamma)||p(\mathcal{G}_x^n)) = \mathcal{L}_{KL_x}^n$ .

Finally, we have the following equation as:

$$\mathcal{I}(\mathcal{G}_x^c, \mathcal{G}_x^n) \leq \min(\mathcal{L}_{KL_x}^c, \mathcal{L}_{KL_x}^n) \quad (20)$$

**The solution to Eq (17).** To reduce the difficulty of mutual information computation in Eq (17), we decompose probability distributions  $p(\mathcal{G}^c|\mathcal{G}, \gamma)$  and  $p(\mathcal{G}^c)$  into variational approximation and multivariate Bernoulli distribution, respectively.

We redefine  $p(\mathcal{G}^c)$  using the variational approximation  $\omega(\mathcal{G}^c)$ , represented by  $e_{ik}$ .  $\omega(\mathcal{G}^c) = e_{ik}^{|\mathcal{G}^{s_i}|} (1 - e_{ik}^{|\mathcal{G}^{s_i}|/|\mathcal{G}^{s_k}|})$ . Inspired by [38], we parameterize  $p(\mathcal{G}_x^c|\mathcal{G}_x, \gamma)$  as a multivariate Bernoulli distribution:

$$p(\mathcal{G}_x^c|\mathcal{G}_x, \gamma) = \prod_{\mathcal{G}_x^{s_i} \in \mathcal{G}_x^c} p_x^c \cdot \prod_{\mathcal{G}_x^{s_i} \notin \mathcal{G}_x^c} (1 - p_x^c) \quad (21)$$

where  $p_x^c$  is the probability distribution given  $\mathcal{G}_x$  and  $\gamma$ , which can be computed via  $p(\mathcal{G}_x^c|\mathcal{G}_x, \gamma)$ .

$$p_x^c = p(\mathcal{G}_x^c|\mathcal{G}_x, \gamma) = \sigma(\mathcal{Z}(\mathcal{G}_x^c), (\mathcal{Z}(\mathcal{G}_x^{n_1}) || \dots || \mathcal{Z}(\mathcal{G}_x^{n_i}))) \quad (22)$$

where  $\sigma(*)$  is a sigmoid function. Therefore, the  $\mathcal{L}_{KL_x}^c$  in Eq (17) is calculated as follows:

$$\begin{aligned} \mathcal{L}_{KL_x}^c &= KL[p(\mathcal{G}_x^c|\mathcal{G}_x, \gamma)||\omega(\mathcal{G}^c)] \\ &= \mathbb{E}_{\sim \mathcal{G}_x^c, \mathcal{G}_x} \left[ \sum p_x^c \log \frac{p_x^c}{e} + (1 - p_x^c) \log \frac{1 - p_x^c}{1 - e} \right] \end{aligned} \quad (23)$$

Similarly, we can obtain the  $\mathcal{L}_{KL_y}^n$ ,  $\mathcal{L}_{KL_y}^c$  and  $\mathcal{L}_{KL_y}^n$ .

3) *The Lower Bound of  $\mathcal{I}(\mathcal{Y}; \mathcal{G}_x^c, \mathcal{G}_y^c)$  in Eq (14):* We compute the lower bound of  $\mathcal{I}(\mathcal{Y}; \mathcal{G}_x^c, \mathcal{G}_y^c)$  using the given graph pair  $(\mathcal{G}_x, \mathcal{G}_y)$  and the label  $\mathcal{Y}$ .

**Proposition III.2. (Lower bound of  $\mathcal{I}(\mathcal{Y}; \mathcal{G}_x^c, \mathcal{G}_y^c)$ )** Given a graph pair  $(\mathcal{G}_x, \mathcal{G}_y)$ , its label information  $\mathcal{Y}$ , and the learned core subgraphs  $(\mathcal{G}_x^c, \mathcal{G}_y^c)$ , we have:

$$\begin{aligned} \mathcal{I}_{ca} &= \mathcal{I}(\mathcal{Y}; \mathcal{G}_x^c, \mathcal{G}_y^c) \\ &= H(\mathcal{Y}) + \int p(\mathcal{Y}) \iint \mathcal{F}_{ca}(\mathcal{G}_x^c, \mathcal{G}_y^c|\mathcal{Y}) d\mathcal{G}_x^c d\mathcal{G}_y^c d\mathcal{Y} \\ &\geq \int p(\mathcal{Y}) \left( \iint \mathcal{F}_{ca}(\mathcal{G}_x^c, \mathcal{G}_y^c|\mathcal{Y}) d\mathcal{G}_x^c d\mathcal{G}_y^c d\mathcal{Y} \right) \\ &:= \frac{1}{NM} \sum_{n=1}^N \sum_{m=1}^M q(\gamma(\mathcal{G}_{x_n}^c, \mathcal{G}_{y_m}^c)|\mathcal{Y}) \\ &= -\mathcal{L}_{pred} \\ \mathcal{F}_{ca}(\mathcal{G}_x^c, \mathcal{G}_y^c|\mathcal{Y}) &= q(\mathcal{G}_x^c, \mathcal{G}_y^c|\mathcal{Y}) \log \left( \frac{p(\mathcal{G}_x^c, \mathcal{G}_y^c|\mathcal{Y})}{q(\mathcal{G}_x^c, \mathcal{G}_y^c)} \right) \end{aligned} \quad (24)$$

where  $q(\mathcal{G}_x^c, \mathcal{G}_y^c|\mathcal{Y})$  is the variational approximation distribution used to approximate the posterior distribution  $p()$ .

The Eq (24) indicates that minimizing the prediction loss  $\mathcal{L}_{pred}$  achieves the minimization of  $-\mathcal{I}(\mathcal{Y}; \mathcal{G}_x^c, \mathcal{G}_y^c)$ .

**The proof of Eq (24).** For the term  $\mathcal{I}_{ca} = \mathcal{I}(\mathcal{Y}; \mathcal{G}_x^c, \mathcal{G}_y^c)$ , by definition:

$$\mathcal{I}_{ca} = \iiint p(\mathcal{Y}, \mathcal{G}_x^c, \mathcal{G}_y^c) \log \left( \frac{p(\mathcal{Y}, \mathcal{G}_x^c, \mathcal{G}_y^c)}{p(\mathcal{Y})} \right) d\mathcal{Y} d\mathcal{G}_x^c d\mathcal{G}_y^c \quad (25)$$

We introduce the variational approximation distribution  $q(\mathcal{G}_x^c, \mathcal{G}_y^c|\mathcal{Y})$  to approximate the conditional probability distribution  $p(\mathcal{G}_x^c, \mathcal{G}_y^c|\mathcal{Y})$ . Then, the  $\mathcal{I}_{ca}$  is expressed as:

$$\begin{aligned} \mathcal{I}_{ca} &= \int p(\mathcal{Y}) \iint q(\mathcal{G}_x^c, \mathcal{G}_y^c|\mathcal{Y}) \log \left( \frac{p(\mathcal{Y}, \mathcal{G}_x^c, \mathcal{G}_y^c)}{q(\mathcal{G}_x^c, \mathcal{G}_y^c)} \right) d\mathcal{Y} d\mathcal{G}_x^c d\mathcal{G}_y^c \\ &= \int p(\mathcal{Y}) \iint q(\mathcal{G}_x^c, \mathcal{G}_y^c|\mathcal{Y}) \log \left( \frac{p(\mathcal{Y}) p(\mathcal{G}_x^c, \mathcal{G}_y^c|\mathcal{Y})}{q(\mathcal{G}_x^c, \mathcal{G}_y^c)} \right) d\mathcal{Y} d\mathcal{G}_x^c d\mathcal{G}_y^c \\ &= \int p(\mathcal{Y}) (\log p(\mathcal{Y}) + \iint \mathcal{F}_{ca}(\mathcal{G}_x^c, \mathcal{G}_y^c|\mathcal{Y}) d\mathcal{G}_x^c d\mathcal{G}_y^c d\mathcal{Y}) \\ &= \int p(\mathcal{Y}) \log p(\mathcal{Y}) d\mathcal{Y} \\ &\quad + \int p(\mathcal{Y}) \iint \mathcal{F}_{ca}(\mathcal{G}_x^c, \mathcal{G}_y^c|\mathcal{Y}) d\mathcal{G}_x^c d\mathcal{G}_y^c d\mathcal{Y} \\ &= H(\mathcal{Y}) + \int p(\mathcal{Y}) \iint \mathcal{F}_{ca}(\mathcal{G}_x^c, \mathcal{G}_y^c|\mathcal{Y}) d\mathcal{G}_x^c d\mathcal{G}_y^c d\mathcal{Y} \end{aligned} \quad (26)$$

$H(\mathcal{Y})$  is the entropy of  $\mathcal{Y}$ . Finally, we have the following equation as:

$$\mathcal{I}(\mathcal{Y}; \mathcal{G}_x^c, \mathcal{G}_y^c) \geq \int p(\mathcal{Y}) \iint \mathcal{F}_{ca}(\mathcal{G}_x^c, \mathcal{G}_y^c|\mathcal{Y}) d\mathcal{G}_x^c d\mathcal{G}_y^c d\mathcal{Y} \quad (27)$$

**The solution to Eq (24).** The prediction term  $q(\gamma(\mathcal{G}_x^c, \mathcal{G}_y^c)|\mathcal{Y})$  in Eq (24) emphasizes leveraging the core substructure pair  $(\mathcal{G}_x^c, \mathcal{G}_y^c)$  to predict the relationship between molecules  $\mathcal{G}_x$  and  $\mathcal{G}_y$ .

According to Eq (15), the embedding representations of molecules  $\mathcal{G}_x$  and  $\mathcal{G}_y$ , composed of their core substructures, are expressed as  $\mathcal{H}_x$  and  $\mathcal{H}_y$ , respectively. Finally, the prediction loss  $\mathcal{L}_{pred}$  of ReAlignFit is denoted as:

$$\mathcal{L}_{pred} = \frac{-1}{MN} \mathbb{E}_{(\mathcal{G}_x, \mathcal{G}_y) \sim \mathcal{Y}} [\log(\sigma(\mathcal{H}_x, \mathcal{H}_y))|\mathcal{Y}] \quad (28)$$

In MRL,  $\mathcal{L}_{pred}$  can be chosen as the cross-entropy loss for Drug-Drug Interaction (DDI) prediction or the mean absolute error loss for Molecular Interaction (MI) prediction.

### C. Model Analysis

We train ReAlignFit by the iterative optimization between SRIN and DRAM. The pseudocode is provided in Algorithm 1. The computational complexity of ReAlignFit is mainly derived from iterative optimization. The complexity of SRIN is  $\mathcal{O}(T_1 \cdot L \cdot |N|^2)$ , and that of DRAM is  $\mathcal{O}(T_2 \cdot J^2)$ .  $T$  represents the number of iterations,  $L$  is GNN layers. Consequently, the overall computational complexity of ReAlignFit is approximately  $\mathcal{O}(T_1 \cdot L \cdot |N|^2 + T_2 \cdot J^2)$ . Owing to  $J \ll N$ , the added computational overhead is still manageable.

## IV. EXPERIMENTS

In this section, we validate the prediction performance of ReAlignFit in two types of tasks on nine datasets. By analyzing and summarizing the relevant experiments, we aim to answer the following research questions:

- **RQ1:** How does the performance of ReAlignFit in MRL, and whether it is susceptible to backbone?
- **RQ2:** Can ReAlignFit improve the stability of MRL in distribution-shifted data?

**Algorithm 1** ReAlignFit

**Input:** Dataset  $\mathcal{D} = (\mathcal{G}_x, \mathcal{Y}, \mathcal{G}_y)$ , SRIN training epochs  $T_1$ , DRAM training epochs  $T_2$ , Model training iterations  $T$

**Output:** Prediction result  $\hat{\mathcal{Y}}$

```

1: Convert SMILES sequences into graph structures;
2: Initialize training parameters;
3: for  $t = 1$  to  $T$  do
4:   for  $t_1 = 1$  to  $T_1$  do
5:     Compute substructure embeddings  $\mathcal{Z}(\mathcal{G}^s)$  by Eq (9);

6:   Obtain interaction-optimized substructure representations  $\mathcal{Z}(\mathcal{G}'^s)$  based on Eqs (10) and (11);
7:   end for
8:   for  $t_2 = 1$  to  $T_2$  do
9:     Generate reconstructed substructures  $\mathcal{Z}(\mathcal{G}^{news})$  via  $e_{ik}$ ;
10:    Obtain aligned core substructure pairs according to Eqs (12) and (13);
11:    Optimize S-GIB and generate refined substructure pairs with Eqs (23) and (28);
12:    if  $\mathcal{L}$  in Eq (16) converges then
13:      Return the S-GIB-optimized representation  $\mathcal{H}$ ;
14:    else
15:       $t_2 \leftarrow t_2 + 1$ ;
16:    end if
17:  end for
18: end for
19: Output the prediction result  $\hat{\mathcal{Y}}$ , computed from  $\mathcal{H}$ .
```

- **RQ3:** What is the key to ReAlignFit’s performance improvement?
- **RQ4:** How does confounding information affect the performance of ReAlignFit?
- **RQ5:** Can the results of ReAlignFit be visually supported?

#### A. Experimental Setup

1) *Datasets:* Following the related research [2], [8], [15], [39], we conduct extensive Molecular Interaction (MI) prediction and Drug-Drug Interaction (DDI) prediction experiments on nine datasets, as detailed in Table I. Chromophore [40], MNSol [41], FreeSolv [42], CompSol [43], Abraham [44], and CombiSolv [45] are chromophore datasets used to describe the free energy of solutes in solvents. These six datasets are widely used for MI prediction [2], [8], [15]. ZhangDDI [46], HetionetDDI [47], and DrugBankDDI (pay version) [48] are commonly utilized for DDI prediction [30]. Following the setup of related work in MRL [2], [15], we divide the datasets into training, validation, and test sets with the ratio of 6:2:2. For DDI datasets that contain only positive examples, we generated negative samples using rule matching and scaffold clustering methods, respectively. To better simulate the real-world data distribution, we set up in-distribution data (Original) with the same distribution as the original data and two different distribution-shifted data (P1 and P2) for DDI prediction, which were used for ReAlignFit learning.

TABLE I  
DATA STATISTICS FOR DIFFERENT DATASETS.

Dataset		# $G_x$	# $G_y$	#Pairs	#Tra	#Val	#Tes	Task
Chromophore	Absorption	6416	725	17276	10366	3455	3455	MI
	Emission	6412	1021	18141	10885	3628	3628	MI
	Lifetime	2755	247	6960	4176	1392	1392	MI
MNSol	FreeSolv	372	86	2275	1365	455	455	MI
	CompSol	560	1	560	336	112	112	MI
	Abraham	442	259	3548	2130	709	709	MI
	CombiSolv	1038	122	6091	3655	1218	1218	MI
		1495	326	10145	6087	2029	2029	MI
ZhangDDI	HetionetDDI	544	544	40255	48306	16102	16102	DDI
	DrugBankDDI	696	696	6410	7692	2564	2564	DDI
		2045	2045	291822	350186	116729	116729	DDI

- **In-Distribution Data (Original):** The original data generated negative samples based on rule matching and is randomly divided into training, validation, and test sets.
- **Rule-based Partitioning (P1):** We generated negative samples for original data based on rule matching and partitioned them by ID to ensure that at least one drug doesn’t repeat in training, validation, and test sets. P1 simulates application scenarios of discovering unknown interactions in existing molecules, such as drug repurposing.
- **Scaffold-based Partitioning (P2):** We generated negative samples for the original data based on scaffold clustering. We used METIS [49] to iteratively partition the drug interaction graph, ensuring that molecules in training, validation, and test sets are entirely distinct. P2 simulates scenarios of discovering interactions between previously unknown molecules, such as drug discovery.

2) *Evaluation Metrics:* In this study, we consider MI prediction and DDI prediction as regression and classification tasks, respectively. Root Mean Square Error (RMSE) and Mean Absolute Error (MAE) are commonly used metrics in regression prediction. Considering the high positive correlation between RMSE and MAE, we employ RMSE for performance evaluation in MI prediction. We assess model performance for DDI prediction based on classification evaluation metrics, including Area Under the Receiver Operating Characteristic Curve (AUROC), Accuracy (ACC), F1-score (F1), Precision (Pre), and Area Under the Precision-Recall Curve (AUPR).

3) *Training Details:* In all experiments, we employ a three-layer MPNN as the encoder to extract molecular feature representations and train ReAlignFit based on two NVIDIA GeForce RTX 4090 24G GPUs. We optimize the parameters using the Adam optimizer and train the model for 50 epochs. The batch size is 128, and the dropout rate is 0.1. For other hyperparameters, we choose from a specific range: learning rate  $lr \in \{0.01, 0.005, 0.001, 0.0005, 0.0001\}$ , both  $\alpha$  and  $\beta$  are selected from  $\{0.5, 0.3, 0.1, 0.01, 0.001\}$ , and the iterations is searched from  $\{1, 3, 5, 10, 15\}$ . The code of ReAlignFit will be publicly available after the paper is accepted.

#### B. Overall Performance (RQ1)

We compare ReAlignFit with four backbone models four backbone models (GCN [36], GAT [35], MPNN [34], and GIN [33]), three molecular representation-based models (CI-GIN [50], MIRACLE [26], and MMGNN [8]), and five

TABLE II  
THE PERFORMANCE OF REALIGNFIT AND COMPARATIVE METHODS IN MI PREDICTION, WITH THE BEST RESULTS HIGHLIGHTED IN **BOLD** AND THE SECOND RESULTS HIGHLIGHTED IN **TEXT**.

Model	Chromophore			MNSol	FreeSolv	CompSol	Abraham	CombiSolv
	Absorption	Emission	Lifetime					
No Representational Alignment								
GCN(ICLR'17)	25.75±1.48	31.87±1.70	0.866±0.015	0.675±0.021	1.192±0.042	0.389±0.009	0.738±0.041	0.672±0.022
GAT(ICLR'18)	26.19±1.44	30.90±1.01	0.859±0.016	0.731±0.007	1.280±0.049	0.387±0.010	0.798±0.038	0.662±0.021
MPNN(ICML'17)	24.43±1.55	30.17±0.99	0.802±0.024	0.682±0.017	1.159±0.032	0.359±0.011	0.601±0.035	0.568±0.005
GIN(ICLR'19)	24.92±1.67	32.31±0.26	0.829±0.027	0.669±0.017	1.015±0.041	0.331±0.016	0.648±0.024	0.595±0.014
CIGIN(AAAI'20)	19.32±0.35	25.09±0.32	0.804±0.010	0.607±0.024	0.905±0.014	0.308±0.018	0.411±0.008	0.451±0.009
Representational Alignment by Attention-based Inductive Bias								
CMRL(KDD'23)	17.93±0.31	24.30±0.22	0.776±0.007	0.551±0.017	0.815±0.046	0.255±0.011	0.374±0.011	0.421±0.008
CGIB(ICML'23)	18.11±0.20	23.90±0.35	0.771±0.005	0.538±0.007	0.852±0.022	0.276±0.017	0.390±0.006	0.422±0.005
MMGNN(IJCAI'24)	18.65±0.34	25.33±0.43	0.801±0.007	0.546±0.011	0.902±0.026	0.267±0.012	0.385±0.008	0.303±0.033
ReAlignFit	16.82±0.25	22.95±0.33	0.769±0.005	0.541±0.010	0.799±0.034	0.261±0.013	0.371±0.008	0.419±0.008
ReAlignFit <sub>GCN</sub>	17.23±0.27	23.35±0.29	0.771±0.007	0.539±0.012	0.796±0.035	0.257±0.016	0.375±0.012	0.316±0.006
ReAlignFit <sub>GAT</sub>	17.55±0.23	23.98±0.36	0.776±0.007	0.543±0.021	0.806±0.036	0.254±0.012	0.381±0.013	0.421±0.009
ReAlignFit <sub>GIN</sub>	17.92±0.46	24.10±0.34	0.772±0.007	0.552±0.037	0.803±0.025	0.267±0.021	0.386±0.017	0.318±0.008

TABLE III  
THE PERFORMANCE OF REALIGNFIT AND COMPARATIVE METHODS IN DDI PREDICTION, WITH THE BEST RESULTS HIGHLIGHTED IN **BOLD** AND THE SECOND RESULTS HIGHLIGHTED IN **TEXT**.

Model	ZhangDDI					HetionteDDI					DrugBankDDI				
	ACC	AUROC	F1	Pre	AUPR	ACC	AUROC	F1	Pre	AUPR	ACC	AUROC	F1	Pre	AUPR
<b>No Representational Alignment</b>															
GCN(ICLR'17)	83.31	91.64	82.91	77.67	91.33	87.62	92.91	90.07	84.66	91.26	84.02	90.96	82.87	80.04	88.36
GAT(ICLR'18)	84.14	92.10	83.42	78.45	91.21	87.94	94.35	89.78	83.52	92.83	84.33	91.26	83.34	80.58	89.13
MPNN(ICML'17)	84.56	92.34	83.32	78.15	91.46	88.73	95.13	89.52	83.66	93.21	87.30	95.90	88.53	80.73	95.08
GIN(ICLR'19)	85.59	93.16	85.07	79.82	92.11	87.37	93.01	87.91	84.05	91.23	85.21	92.58	85.88	83.57	90.92
MIRACLE(WWW'21)	84.90	93.05	83.94	77.81	91.25	87.01	92.88	87.34	83.91	90.88	84.98	92.17	85.43	83.22	90.28
CIGIN(AAAI'20)	85.54	93.28	84.36	80.23	91.89	90.87	92.77	90.33	88.98	94.62	91.02	93.62	91.18	89.35	94.88
<b>Representational Alignment by Attention-based Inductive Bias</b>															
SSI-DDI(BIB'21)	85.35	93.14	81.96	78.97	92.09	87.95	93.83	88.56	84.28	91.60	84.16	91.23	84.64	82.13	89.47
DSN-DDI(BIB'23)	86.65	91.13	87.86	84.33	86.42	91.25	95.31	91.59	89.52	94.66	90.49	96.15	90.58	89.76	95.27
SA-DDI(CS'22)	77.31	50.26	45.06	52.54	29.97	91.00	<b>95.89</b>	91.26	88.39	94.96	92.60	95.33	92.80	90.38	96.62
CMRL(KDD'23)	86.32	93.73	87.68	84.01	91.56	91.25	93.18	91.53	91.23	95.24	92.26	95.05	92.43	90.30	95.96
CGIB(ICML'23)	86.36	93.78	87.24	83.91	91.88	91.08	93.26	91.35	91.55	94.89	92.37	94.98	92.03	90.65	96.11
MMGNN(IJCAI'24)	85.33	93.23	86.45	84.36	90.89	90.67	94.34	90.75	92.22	<b>95.28</b>	93.61	95.12	92.38	91.22	95.39
ReAlignFit	<b>89.43</b>	95.68	<b>90.88</b>	<b>87.68</b>	<b>93.36</b>	<b>92.39</b>	<b>97.17</b>	<b>92.62</b>	<b>95.48</b>	<b>96.05</b>	<b>95.53</b>	96.31	94.59	<b>94.38</b>	97.05
ReAlignFit <sub>GCN</sub>	87.62	<b>95.69</b>	90.34	87.54	92.81	91.16	94.22	91.55	92.29	95.21	<b>95.62</b>	97.95	<b>95.62</b>	94.37	<b>97.09</b>
ReAlignFit <sub>GAT</sub>	<b>88.35</b>	94.22	90.41	86.92	91.76	91.66	94.56	91.76	91.97	95.03	95.35	<b>98.42</b>	93.87	93.67	96.26
ReAlignFit <sub>GIN</sub>	85.23	94.35	89.34	86.89	90.67	92.12	92.95	91.91	93.04	95.23	93.33	98.09	95.01	91.58	95.82

substructure representation-based models (SSI-DDI [51], SA-DDI [21], DSN-DDI [16], CMRL [2], and CGIB [15]) in MI and DDI tasks. The MI prediction and DDI prediction results are presented in Table II and Table III, respectively.

**Comprehensive Analysis:** ReAlignFit demonstrates the best overall performance in MI prediction and DDI prediction. Particularly, ReAlignFit achieves an average improvement of 2.7% in ACC and 3.0% in AUROC in three DDI datasets. Additionally, ReAlignFit achieves the best prediction performance in multiple MI datasets, reducing RMSE by 1.83 and 2.38 of Absorption and Emission attributes on the Chromophore dataset, respectively. This result suggests that incorporating domain knowledge into MRL and substructure representational alignment contributes to improving the model's predictive performance.

**Importance Analysis of Representational Alignment:** The prediction performance of methods considering representational alignment (CGIB, MMGNN, ReAlignFit, etc.) is

significantly better than those that ignore it. Whether it is DDI or MI prediction, the model performance improvement by representational alignment is noticeable. This result indicates representational alignment is a critical factor in molecular relationships. However, it is worth noting that representational alignment methods by attention-based inductive bias achieve an average improvement of less than 5% on the Chromophore dataset, whereas ReAlignFit exceeds 8.5%. This observation is consistent with the nature of the Induced Fit, emphasising dynamic conformational changes of substructures.

**ReAlignFit Compatibility Analysis:** By substituting different GNN models within ReAlignFit, we observe that its performance fluctuates slightly. ReAlignFit, combined with different GNN backbones, consistently achieved the best or second-best predictive performance in all evaluation metrics for FreeSolv, CompSol, ZhangDDI and DrugBankDDI datasets. This result indicates that ReAlignFit is less affected by the backbone, demonstrating flexibility in integration with general graph



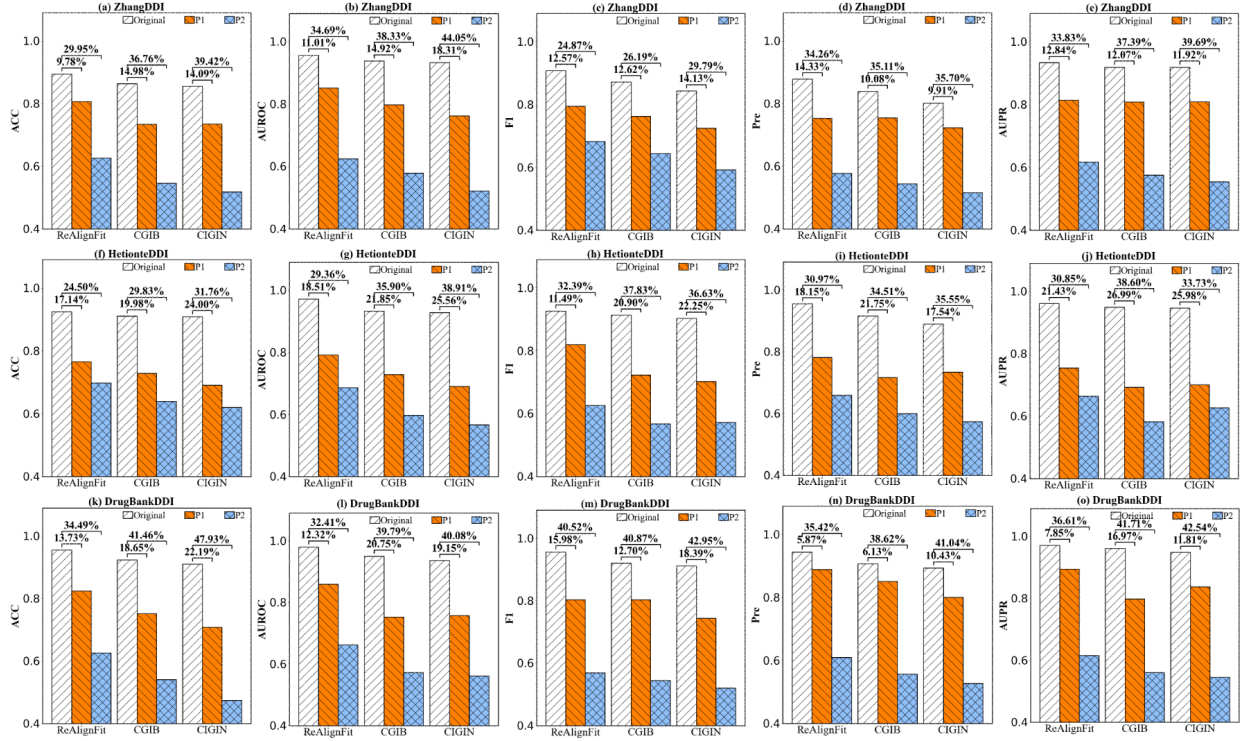


Fig. 3. The performance and RPD of ReAlignFit, CGIB and CIGIN in different data distributions.

models. Furthermore, this highlights ReAlignFit’s reliable applicability at the model level.

### C. Stability Analysis (RQ2)

In this section, we analyze the stability of model prediction performance in distribution-shifted data. To validate the model’s performance in different data distributions, we quantify model stability by calculating the Relative Performance Degradation (RPD) for AUROC, ACC, F1, Pre, and AUPR. RPD is defined as follows:

$$RPD_M = \frac{|Eva_M^{P_i} - Eva_M^{Ori}|}{Eva_M^{Ori}} \times 100\% \quad (29)$$

where  $Eva$  represents the evaluation metrics.  $Eva_M^P$  and  $Eva_M^{Ori}$  denote the prediction performance in the original and drift distributions, respectively.  $M \in AUROC, ACC, F1, Pre, AUPR$  and  $P_i \in P1, P2$ .

We conduct extensive experiments on the datasets generated by the three data distributions. The experimental results are shown in Fig. 3. The values in Fig. 3 are RPD. We also present the DDI prediction performance of ReAlignFit and comparison models on distribution-shifted data in Table IV. Among these, P1 have the most minor performance differences from the original data, followed by P2.

**Stability Analysis:** Experimental results show that data distribution variations significantly impact the predictive performance of models. ReAlignFit maintains the best stability in different data distributions compared to methods that do not consider representational alignment. Compared to CGIB, ReAlignFit improved ACC prediction stability by at least 4.5% and 6% in two data distribution scenarios. ReAlignFit exhibits the most minor performance degradation and achieves the

highest stability in varying data distributions. ReAlignFit’s performance degradation ranges from 6% to 18% in the P1 scenario, with certain evaluation metrics showing only around 25% decline in P2. In contrast, CGIB and CIGIN experience performance fluctuations exceeding 35% in most metrics on P2. These findings show that stability is the critical factor in the success of ReAlignFit, primarily attributed to DRAM, which identifies chemically functionally compatible core substructure pairs through representational alignment. Comprehensively, representational alignment improves model stability and maintains strong predictive performance in distribution-shifted datasets. This directly confirms the role of representational alignment in improving the stability of MRL.

**Predictive Performance Analysis:** With increasing distribution differences, all models exhibit varying degrees of performance degradation, highlighting that data distribution shifts remain a significant challenge for MRL. Encouragingly, ReAlignFit consistently outperforms other comparison models in DDI prediction in the P2 data scenario. Moreover, ReAlignFit outperforms the second-best method in three datasets on the P1 data scenario by 5.07%, 3.67%, 5.19% in ACC, and 3.32%, 6.05%, 1.87% in AUROC. These results provide the possibility of applying ReAlignFit in molecular science. By comprehensively analyzing the experimental results of ReAlignFit in distribution drift scenarios, we can see that ReAlignFit exhibits better prediction performance and stability in distribution-shifted data. We attribute the results to two main reasons: substructure representational alignment identifies substructure pairs that contain stable causal information. On the other hand, ReAlignFit mitigates the impact of confounding substructures on molecular representations by weakening the association of confounding substructures with causal substructures.

TABLE IV  
THE DDI PREDICTION PERFORMANCE OF REALIGNFIT AND COMPARISON MODELS IN DISTRIBUTIONAL DRIFT DATA, WITH THE BEST RESULTS HIGHLIGHTED IN **BOLD** AND THE SECOND RESULTS HIGHLIGHTED IN **TEXT**.

Model	ZhangDDI					HetionteDDI					DrugBankDDI				
	ACC	AUROC	F1	Pre	AUPR	ACC	AUROC	F1	Pre	AUPR	ACC	AUROC	F1	Pre	AUPR
<b>Rule-based Partitioning (P1)</b>															
GCN	65.84	71.31	65.46	66.46	69.94	66.95	68.13	70.08	60.19	65.67	61.15	72.58	72.62	63.45	69.87
GAT	68.38	70.79	67.75	66.89	65.94	67.88	68.98	73.61	64.05	66.37	62.18	73.04	74.11	61.96	67.56
MPNN	68.34	67.64	67.82	64.96	62.27	68.03	69.57	72.57	65.32	65.39	66.51	70.43	74.02	60.47	64.02
GIN	70.15	71.38	71.83	66.99	66.09	69.03	68.88	72.26	66.09	66.33	66.93	71.23	74.67	61.22	65.21
MIRACLE	72.46	71.31	71.92	65.90	64.41	69.56	70.30	70.95	65.36	65.99	68.57	71.14	75.32	62.03	64.04
CIGIN	73.49	76.20	72.44	72.28	80.94	69.06	69.11	70.23	73.37	70.01	70.82	75.69	74.41	80.03	83.67
SSI-DDI	71.87	75.00	67.12	71.72	74.19	68.30	69.85	72.16	64.51	69.62	64.47	75.69	53.72	77.03	73.70
DSN-DDI	72.62	79.83	69.00	72.40	<b>81.66</b>	69.92	68.10	74.98	74.90	70.04	77.22	84.01	72.73	<b>90.59</b>	87.90
CMRL	73.75	76.82	75.05	74.41	81.54	69.66	67.19	70.02	68.86	68.23	72.68	73.27	72.90	81.63	74.22
CGIB	73.42	79.79	76.23	<b>75.45</b>	80.79	72.88	72.15	72.26	71.64	69.28	75.14	75.27	<b>80.34</b>	85.09	79.80
MMGNN	72.87	74.95	74.47	74.90	78.05	69.52	73.14	73.80	71.07	67.49	71.78	76.26	72.88	83.52	79.01
ReAlignFit	<b>78.82</b>	<b>83.15</b>	<b>79.46</b>	75.27	81.37	<b>76.55</b>	<b>79.19</b>	<b>81.98</b>	<b>78.15</b>	<b>75.47</b>	<b>82.41</b>	<b>85.88</b>	78.97	88.84	<b>89.47</b>
<b>Scaffold-based Partitioning (P2)</b>															
GCN	47.04	44.36	51.58	51.56	54.44	58.22	53.82	53.06	51.32	62.46	43.15	41.18	46.20	51.29	50.17
GAT	49.94	47.42	55.34	52.90	56.87	61.42	53.88	55.68	53.92	61.32	43.44	45.61	51.20	50.06	52.30
MPNN	46.81	45.15	53.91	51.59	53.14	63.07	55.25	55.98	53.32	60.84	46.50	45.08	52.66	52.95	53.26
GIN	52.25	44.35	58.52	52.17	51.14	63.13	54.83	52.38	54.14	60.43	45.13	41.85	<b>54.95</b>	52.27	51.38
MIRACLE	45.47	48.34	59.09	51.31	48.91	<b>64.14</b>	54.06	<b>57.66</b>	54.19	59.68	42.57	47.33	53.12	53.77	53.49
CIGIN	51.82	52.19	59.23	51.59	55.42	62.01	56.67	57.24	57.35	62.70	47.39	56.10	52.02	52.68	54.52
SSI-DDI	49.32	49.92	62.92	48.83	55.16	61.64	56.61	58.44	54.04	<b>67.70</b>	45.75	54.77	53.96	54.62	54.59
DSN-DDI	48.78	47.17	63.51	54.78	47.33	61.72	55.11	52.45	53.72	61.27	46.08	<b>57.44</b>	53.49	52.28	55.71
CMRL	53.70	56.79	<b>65.39</b>	<b>54.80</b>	<b>57.84</b>	63.83	56.17	55.42	55.81	60.69	52.61	57.16	54.36	54.25	54.53
CGIB	<b>54.61</b>	<b>57.83</b>	<b>64.39</b>	<b>54.45</b>	<b>57.53</b>	63.91	59.78	56.79	<b>59.96</b>	58.26	54.07	57.19	54.42	<b>55.64</b>	<b>56.02</b>
MMGNN	52.02	56.81	65.31	53.95	56.16	64.08	<b>60.47</b>	56.26	59.09	57.65	<b>54.29</b>	56.74	52.11	51.65	51.31
ReAlignFit	<b>60.85</b>	<b>59.49</b>	<b>68.28</b>	<b>57.76</b>	<b>61.78</b>	<b>69.75</b>	<b>68.64</b>	<b>62.62</b>	<b>65.91</b>	67.73	<b>62.58</b>	<b>66.20</b>	<b>56.87</b>	<b>60.95</b>	<b>61.55</b>

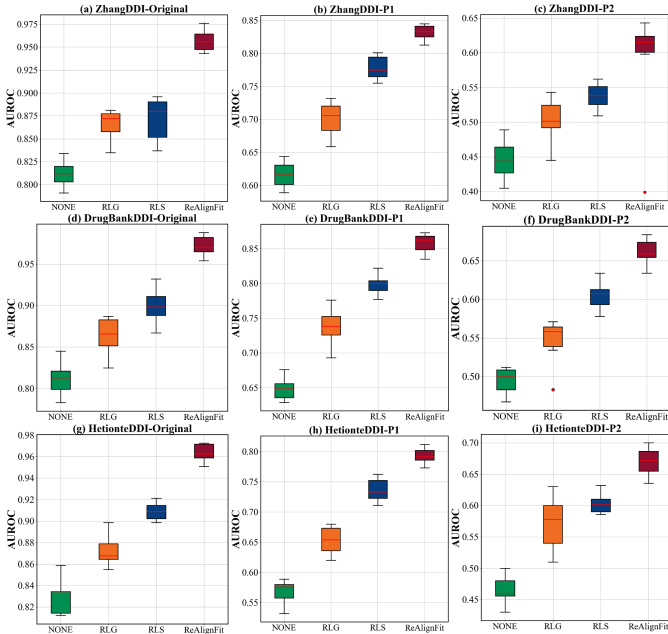


Fig. 4. The experimental results of ablation experiment.

#### D. Ablation Experiment (RQ3)

To analyze the impact of representational alignment and S-GIB on the overall performance of the model, we compared the following model variants: NONE (no representational alignment and optimization), RLG (optimized substructure

representation based on S-GIB), and RLS (optimized substructure representation based on representational alignment). The results are shown in Fig. 4.

- **NONE**: No representational alignment is applied. Relationship prediction relies solely on substructures extracted by SRIN as molecular feature representations.
- **RLG**: S-GIB is used for optimizing substructure representations, focusing on molecular-level alignment and assessing S-GIB’s impact on MRL stability without representational alignment.
- **RLS**: Representational alignment is performed at the substructure level, considering dynamic interactions between substructures for MRL, excluding S-GIB’s optimization.

The experimental results in Fig. 4 demonstrate that incorporating S-GIB optimization and substructure representational alignment improves AUROC by 4%, 8%, 10% and 8%, 16%, 13%, respectively, for the three data distributions in the HetionteDDI dataset. Similar trends are observed in the ZhangDDI and DrugBankDDI datasets. Notably, the performance gains in AUROC achieved by substructure representational alignment are higher than those from S-GIB optimization. These experimental results suggest that representational alignment and S-GIB optimization are critical factors in improving ReAlignFit’s predictive performance.

Comparing the distribution ranges of AUROC of the five ablation experiments in Fig. 4, we observe that the RLS variant exhibits tighter AUROC ranges on distribution-shifted data. This result indicates that substructure representational

alignment effectively enhances model stability. In contrast, the contribution of S-GIB optimization to stability is negligible and even reduces the model stability in individual scenarios. These phenomena suggest that selecting substructure pairs with high functional compatibility through representational alignment is the key to model stability improvement.

Overall, representational alignment improves MRL stability by identifying highly compatible binding sites. S-GIB enhances predictive performance by mitigating the influence of confounding substructures on highly compatible substructures. The synergy between representational alignment and S-GIB optimization achieves a win-win situation regarding model predictive performance and stability.

#### E. Confusion Analysis on $\alpha$ and $\beta$ (RQ4)

To verify the impact of confounding information  $\alpha I(G_x^c, G_x^n) + \beta I(G_y^c, G_y^n)$  in Eq (14) on the stability of ReAlignFit’s predictive performance, we set  $\alpha$  and  $\beta$  to  $\{0.001, 0.01, 0.1, 0.3, 0.5\}$  and conduct relevant experiments in three different data distributions. The experimental results are shown in Fig. 5.

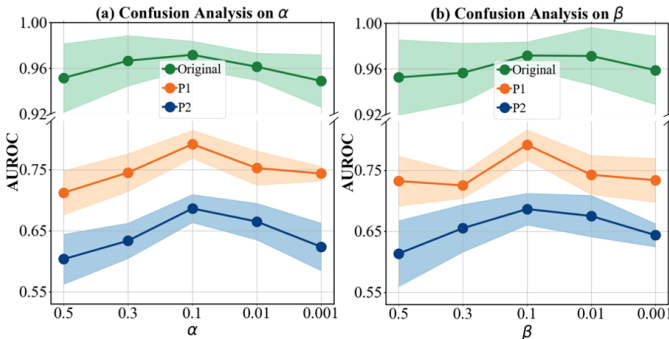


Fig. 5. The experimental results of confusion analysis in HetionteDDI dataset.

In Fig. 5, there exists an optimal value of  $\alpha$  and  $\beta$  (i.e.,  $\alpha = \beta = 0.1$ ) that balances the model’s predictive performance and the impact of confounding information on molecular representation. When  $\alpha$  and  $\beta$  are excessively large ( $\alpha = \beta \geq 0.3$ ), the model’s predictive performance fluctuates significantly in different data distributions, and its stability decreases markedly. This occurs because high values of  $\alpha$  and  $\beta$  cause the model to learn excessive confounding information, making information difficult to use in MRL effectively. Conversely, when  $\alpha$  and  $\beta$  are smaller ( $\alpha = \beta < 0.1$ ), while the model’s performance fluctuations are reduced, its predictive performance remains below optimal levels. In this case, the model struggles to adequately distinguish between confounding and core substructures, consequently affecting its performance and generalization. Therefore, appropriately adjusting  $\alpha$  and  $\beta$  enables the model to more effectively balance the impact of confounding and core information on molecular representation to improve the stability of the model’s prediction performance.

#### F. Visualization Analysis (RQ5)

To validate ReAlignFit’s ability to capture core substructures in MRL, we visualize the node features and the interactions between substructures, as shown in Fig. 6.

In the node feature representations of drug molecules, the substructure information captured by ReAlignFit closely aligns with the actual electrostatic potential of the molecules and emphasizes the interactions between atoms within molecules. As shown in Figs. 6(a), (c) and Figs. 6(d), (f), ReAlignFit demonstrates satisfactory recognition capabilities for multiple complex functional groups within molecules. The Mantel test [52] results shown in the Fig. 6(b) and Fig. 6(e) display the interaction strength between different substructures. Darker and thicker lines represent stronger interactions between substructures. The results indicate the high interaction strength between the symmetrical -COOH groups (green and orange areas) in DB00548 and Group1 (benzene ring) in DB01117. Group4 in DB00802 strongly interacts with the functional group (purple region) in DB00440. This is consistent with the domain knowledge in Induced Fit theory that chemical reactions occur between core substructures. Additionally, the Group3 in DB01117 exhibits a weaker interaction with substructures in DB00548, as shown in Fig. 6. This is due to the inertness of Group3’s cyclic structure, which makes it difficult to react chemically with other substructures. In conclusion, ReAlignFit not only captures substructure information within molecules but also highlights the crucial role of this substructure information in determining the occurrence of chemical reactions. The experimental results provide an effective explanation for ReAlignFit to capture core substructure in MRL.

To further demonstrate the performance of ReAlignFit, we perform dimensionality reduction on the molecular pair features captured by ReAlignFit, as shown in Fig. 7. ReAlignFit distinctly differentiates the interactions among molecular pairs in the three datasets. The visual presentation results confirm ReAlignFit’s satisfactory performance in MRL.

## V. RELATED WORK

### A. Molecular Relational Learning

MRL is an essential task in molecular representation, encompassing various applications [4], [8], [53]. In this paper, we focus on MI and DDI predictions. In molecular interaction prediction, the model primarily predicts changes in chemical properties caused by chemical reactions. CIGIN [50] employed a message-passing network and collaborative attention to encode intra-molecular atoms and predict solvation-free energy. CMRL [2] combined molecular representation with GNNs and causal relationships, identifying substructures causally related to chemical reactions. MMGNN [8] explicitly models chemical bonds between atoms by adding connections within the molecule, ultimately predicting solvent-free energy by attention-based aggregation. DDI prediction focuses on identifying the interaction relationships between drug molecules, which is critical for co-medication in clinical settings [54]. Substructure-based DDI prediction is currently a research hotspot. SA-DDI [21], SSI-DDI [51], and DSN-DDI [16] extract substructure information based on GNNs from drugs in various ways to better represent drug molecules. Additionally, TIGER [30] uses a Transformer architecture with a relation-aware attention mechanism to construct semantic relationships between drugs. From the data perspective, solutions targeting sparse and imbalanced data in DDI tasks



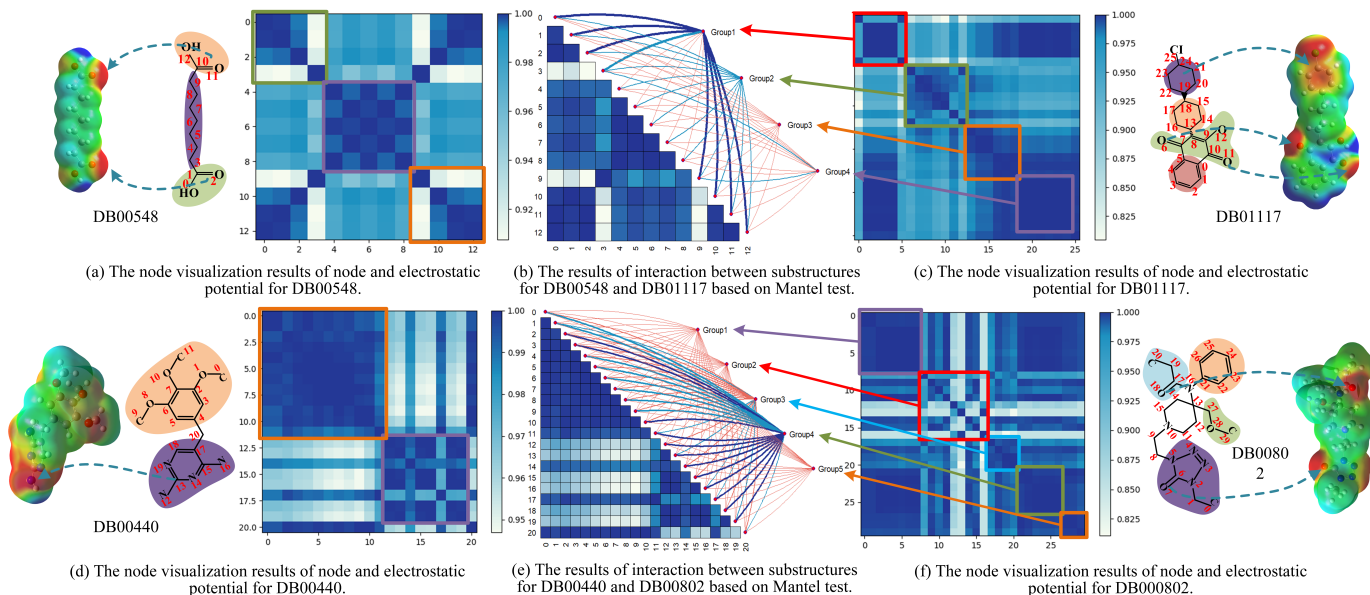


Fig. 6. The visualization of node features and interaction strengths between substructures.

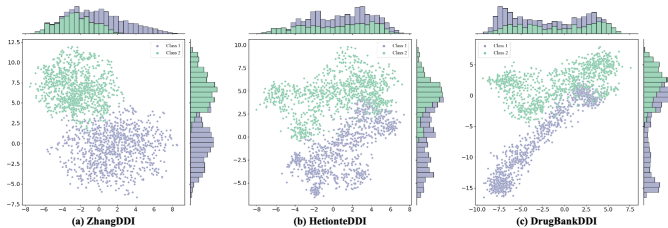


Fig. 7. The visualization of molecular pairs interaction prediction results in the DDI dataset. Class 1 indicates molecular pairs with an interaction, while Class 2 indicates molecular pairs without an interaction.

have been progressively proposed [55], [56]. DDIPrompt [55] combines hierarchical pre-training with prompt learning to encourage an understanding of the drug’s molecular properties. Moreover, researchers have advanced the interpretability of DDI by leveraging extensive drug evaluation [57] and hierarchical views [58]. In summary, the current mainstream of MRL is to utilize graph-based molecular representations while incorporating attention mechanisms to capture interactions between molecular substructures.

### B. Representational Alignment

Representational alignment refines embedding representations to guarantee that input data is coherently and precisely captured within the representation space [59]–[61]. Alignment enhances model performance and reliability in complex environments. In the era of large language models (LLMs), representational alignment has become a critical technology for building LLMs that meet specific human needs [28], [62]. Existing studies primarily introduce alignment through inductive bias, behavior imitation, environmental feedback, and model feedback [28]. In molecular representations, researchers predominantly adopt attention mechanism-based inductive bias to realize representational alignment [63]. Molecular representational alignment is a critical step in models that accurately capture molecules’ structural and functional prop-

erties [13], [64]. Graphormer [65] achieves molecular-level representational alignment through message passing, while CGIB [15] focuses on aligning molecular representations at the substructure level. The Dual-Graph Framework [66] combines molecular-level and substructure-level alignments, integrating the strengths of both approaches.

Existing molecular representational alignment methods rely on attention mechanisms to compute inductive bias, resulting in results that reflect statistical correlations and lack dynamic adaptability. Therefore, we incorporate chemical domain knowledge into ReAlignFit to dynamically align the representations between substructures based on simulated molecular conformational changes to identify substructure pairs with high functional compatibility.

## VI. CONCLUSION

In this paper, we propose the the Representational Alignment with Chemical Induced Fit to improve the stability of MRL. ReAlignFit dynamically aligns representation by introducing Induced Fit-based inductive bias. ReAlignFit simulates dynamic conformational changes during Induced Fit by a self-supervised approach. Additionally, it integrates S-GIB to align core substructure pairs with potential compatibility in chemical functions. Experimental results demonstrate that ReAlignFit achieves the best predictive performance and significantly improves the predictive stability in distribution-shifted data.

In future work, we will explore the deep integration of ReAlignFit with drug discovery and chemical synthesis. Simultaneously, we will focus on leveraging Large Language Model to integrate cross-modal experimental data and optimize computational resource efficiency to promote its deployment in real-world applications.

## REFERENCES

- [1] J. Fang, S. Zhang, C. Wu, Z. Yang, Z. Liu, S. Li, K. Wang, W. Du, and X. Wang, “MolTC: Towards Molecular Relational Modeling In

- Language Models,” in *Proceedings of the 62nd Annual Meeting of the Association for Computational Linguistics*, 2024, pp. 1943–1958.
- [2] N. Lee, K. Yoon, G. S. Na, S. Kim, and C. Park, “Shift-Robust Molecular Relational Learning with Causal Substructure,” in *Proceedings of the 29th ACM SIGKDD Conference on Knowledge Discovery and Data Mining*, 2023, pp. 1200–1212.
  - [3] L. Yang, J. Zheng, H. Wang, Z. Liu, Z. Huang, S. Hong, W. Zhang, and B. Cui, “Individual and Structural Graph Information Bottlenecks for Out-of-Distribution Generalization,” *IEEE Transactions on Knowledge and Data Engineering*, vol. 36, no. 2, pp. 682–693, 2024.
  - [4] H. Pei, T. Chen, A. Chen, H. Deng, J. Tao, P. Wang, and X. Guan, “Hago-Net: Hierarchical Geometric Message Passing for Molecular Representation Learning,” in *Proceedings of the 38th AAAI Conference on Artificial Intelligence*, vol. 38, no. 13, 2024, pp. 14 572–14 580.
  - [5] H. Li, X. Wang, Z. Zhang, and W. Zhu, “OOD-GNN: Out-of-Distribution Generalized Graph Neural Network,” in *Proceedings of the 40th International Conference on Data Engineering*, 2024, pp. 5681–5682.
  - [6] B. Gao, B. Qiang, H. Tan, Y. Jia, M. Ren, M. Lu, J. Liu, W.-Y. Ma, and Y. Lan, “DrugCLIP: Contrastive Protein-Molecule Representation Learning for Virtual Screening,” in *Proceedings of the 37th International Conference on Neural Information Processing Systems*, vol. 36, 2023, pp. 44 595–44 614.
  - [7] R. Wang, H. Dai, C. Yang, L. Song, and C. Shi, “Advancing Molecule Invariant Representation via Privileged Substructure Identification,” in *Proceedings of the 30th ACM SIGKDD Conference on Knowledge Discovery and Data Mining*, 2024, pp. 3188–3199.
  - [8] W. Du, S. Zhang, J. X. Di Wu, Z. Zhao, J. Fang, and Y. Wang, “MMGNN: A Molecular Merged Graph Neural Network for Explainable Solvation Free Energy Prediction,” in *Proceedings of the Thirty-Third International Joint Conference on Artificial Intelligence*, 2024, pp. 5808–5816.
  - [9] D. E. Koshland Jr, “The Key-Lock Theory and the Induced Fit Theory,” *Angewandte Chemie International Edition in English*, vol. 33, no. 23–24, pp. 2375–2378, 1995.
  - [10] M. McGibbon, S. Shave, J. Dong, Y. Gao, D. R. Houston, J. Xie, Y. Yang, P. Schwaller, and V. Blay, “From Intuition to AI: Evolution of Small Molecule Representations in Drug Discovery,” *Briefings in Bioinformatics*, vol. 25, no. 1, p. bbad422, 2024.
  - [11] J. Xia, L. Zhang, X. Zhu, Y. Liu, Z. Gao, B. Hu, C. Tan, J. Zheng, S. Li, and S. Z. Li, “Understanding the Limitations of Deep Models for Molecular Property Prediction: Insights and Solutions,” *Advances in Neural Information Processing Systems*, vol. 36, pp. 64 774–64 792, 2023.
  - [12] K. Maboudi, B. Giri, H. Miyawaki, C. Kemere, and K. Diba, “Retuning of Hippocampal Representations During Sleep,” *Nature*, pp. 1–9, 2024.
  - [13] S. Seo, S. Kim, J. Jung, Y. Lee, and C. Park, “Self-Explainable Temporal Graph Networks based on Graph Information Bottleneck,” in *Proceedings of the 30th ACM SIGKDD Conference on Knowledge Discovery and Data Mining*, 2024.
  - [14] J. Born and M. Manica, “Regression Transformer Enables Concurrent Sequence Regression and Generation for Molecular Language Modelling,” *Nature Machine Intelligence*, vol. 5, no. 4, pp. 432–444, 2023.
  - [15] N. Lee, D. Hyun, G. S. Na, S. Kim, J. Lee, and C. Park, “Conditional Graph Information Bottleneck for Molecular Relational Learning,” in *Proceedings of the 40th International Conference on Machine Learning*, vol. 202, 2023, pp. 18 852–18 871.
  - [16] Z. Li, S. Zhu, B. Shao, X. Zeng, T. Wang, and T.-Y. Liu, “DSN-DDI: An Accurate and Generalized Framework for Drug-Drug Interaction Prediction by Dual-View Representation Learning,” *Briefings in Bioinformatics*, vol. 24, no. 1, p. bbac597, 2023.
  - [17] X. Fang, L. Liu, J. Lei, D. He, S. Zhang, J. Zhou, F. Wang, H. Wu, and H. Wang, “Geometry-Enhanced Molecular Representation Learning for Property Prediction,” *Nature Machine Intelligence*, vol. 4, no. 2, pp. 127–134, 2022.
  - [18] J. Rao, J. Xie, Q. Yuan, D. Liu, Z. Wang, Y. Lu, S. Zheng, and Y. Yang, “A Variational Expectation-Maximization Framework for Balanced Multi-Scale Learning of Protein and Drug Interactions,” *Nature Communications*, vol. 15, no. 1, p. 4476, 2024.
  - [19] S.-W. Li, L.-C. Xu, C. Zhang, S.-Q. Zhang, and X. Hong, “Reaction Performance Prediction with an Extrapolative and Interpretable Graph Model Based on Chemical Knowledge,” *Nature Communications*, vol. 14, no. 1, p. 3569, 2023.
  - [20] N. Yang, K. Zeng, Q. Wu, and J. Yan, “Molerec: Combinatorial Drug Recommendation with Substructure-Aware Molecular Representation Learning,” in *Proceedings of the 32nd ACM on Web Conference*, 2023, pp. 4075–4085.
  - [21] Z. Yang, W. Zhong, Q. Lv, and C. Y.-C. Chen, “Learning Size-Adaptive Molecular Substructures for Explainable Drug-Drug Interaction Prediction by Substructure-Aware Graph Neural Network,” *Chemical Science*, vol. 13, no. 29, pp. 8693–8703, 2022.
  - [22] Z. Yang, W. Zhong, Q. Lv, T. Dong, G. Chen, and C. Y.-C. Chen, “Interaction-Based Inductive Bias in Graph Neural Networks: Enhancing Protein-Ligand Binding Affinity Predictions From 3D Structures,” *IEEE Transactions on Pattern Analysis and Machine Intelligence*, 2024.
  - [23] K.-K. Mak, Y.-H. Wong, and M. R. Pichika, “Artificial Intelligence in Drug Discovery and Development,” *Drug Discovery and Evaluation: Safety and Pharmacokinetic Assays*, pp. 1461–1498, 2024.
  - [24] Y. Hu, D. Stumpfe, and J. Bajorath, “Recent Advances in Scaffold Hopping: Miniperspective,” *Journal of Medicinal Chemistry*, vol. 60, no. 4, pp. 1238–1246, 2017.
  - [25] H.-J. Böhm, A. Flohr, and M. Stahl, “Scaffold Hopping,” *Drug Discovery Today: Technologies*, vol. 1, no. 3, pp. 217–224, 2004.
  - [26] Y. Wang, Y. Min, X. Chen, and J. Wu, “Multi-View Graph Contrastive Representation Learning for Drug-Drug Interaction Prediction,” in *Proceedings of the 30th ACM on Web Conference*, 2021, pp. 2921–2933.
  - [27] X. Su, P. Hu, Z.-H. You, S. Y. Philip, and L. Hu, “Dual-Channel Learning Framework for Drug-Drug Interaction Prediction via Relation-Aware Heterogeneous Graph Transformer,” in *Proceedings of the 38th AAAI Conference on Artificial Intelligence*, vol. 38, no. 1, 2024, pp. 249–256.
  - [28] B. Cao, K. Lu, X. Lu, J. Chen, M. Ren, H. Xiang, P. Liu, Y. Lu, B. He, X. Han *et al.*, “Towards Scalable Automated Alignment of LLMs: A Survey,” *arXiv preprint arXiv:2406.01252*, 2024.
  - [29] J. B. Stiller, R. Otten, D. Häussinger, P. S. Rieder, D. L. Theobald, and D. Kern, “Structure Determination of High-Energy States in a Dynamic Protein Ensemble,” *Nature*, vol. 603, no. 7901, pp. 528–535, 2022.
  - [30] K. Zhang, F. Huang, L. Liu, Z. Xiong, H. Zhang, Y. Qian, and W. Zhang, “Heterogeneous Causal Metapath Graph Neural Network for Gene-Microbe-Disease Association Prediction,” in *Proceedings of the 33rd International Joint Conference on Artificial Intelligence*, 2024.
  - [31] D. Weininger, “SMILES, a Chemical Language and Information System. 1. Introduction to Methodology and Encoding Rules,” *Journal of Chemical Information and Computer Sciences*, vol. 28, no. 1, p. 31–36, 1988.
  - [32] N. Brown, *In Silico Medicinal Chemistry: Computational Methods to Support Drug Design*. Royal Society of Chemistry, 2015.
  - [33] K. Xu, W. Hu, J. Leskovec, and S. Jegelka, “How Powerful are Graph Neural Networks?” in *Proceedings of the 7th International Conference on Learning Representations*, 2019.
  - [34] J. Gilmer, S. S. Schoenholz, P. F. Riley, O. Vinyals, and G. E. Dahl, “Neural Message Passing for Quantum Chemistry,” in *Proceedings of the 34th International Conference on Machine Learning*, 2017, p. 1263–1272.
  - [35] P. Veličković, G. Cucurull, A. Casanova, A. Romero, P. Lio, and Y. Bengio, “Graph Attention Networks,” in *Proceedings of the 6th International Conference on Learning Representations*, 2018.
  - [36] T. N. Kipf and M. Welling, “Semi-Supervised Classification with Graph Convolutional Networks,” in *Proceedings of the 5th International Conference on Learning Representations*, 2017.
  - [37] S. Hu, Z. Lou, X. Yan, and Y. Ye, “A Survey on Information Bottleneck,” *IEEE Transactions on Pattern Analysis and Machine Intelligence*, 2024.
  - [38] S. Seo, S. Kim, J. Jung, Y. Lee, and C. Park, “Self-Explainable Temporal Graph Networks based on Graph Information Bottleneck,” in *Proceedings of the 30th ACM SIGKDD Conference on Knowledge Discovery and Data Mining*, ser. KDD ’24, 2024, p. 2572–2583.
  - [39] M. Boulougouri, P. Vanderghenst, and D. Probst, “Molecular Set Representation Learning,” *Nature Machine Intelligence*, vol. 6, pp. 754–763, 2024.
  - [40] J. F. Joung, M. Han, M. Jeong, and S. Park, “Experimental Database of Optical Properties of Organic Compounds,” *Scientific Data*, vol. 7, no. 1, p. 295, 2020.
  - [41] A. V. Marenich, C. P. Kelly, J. D. Thompson, G. D. Hawkins, C. C. Chambers, D. J. Giesen, P. Winget, C. J. Cramer, and D. G. Truhlar, “Minnesota Solvation Database (MNSOL) Version 2012,” 2020.
  - [42] D. L. Mobley and J. P. Guthrie, “FreeSolv: A Database of Experimental and Calculated Hydration Free Energies, with Input Files,” *Journal of Computer-Aided Molecular Design*, vol. 28, pp. 711–720, 2014.
  - [43] E. Moine, R. Privat, B. Sirjean, and J.-N. Jaubert, “Estimation of Solvation Quantities from Experimental Thermodynamic Data: Development of the Comprehensive CompSol Databank for Pure and Mixed Solutes,” *Journal of Physical and Chemical Reference Data*, vol. 46, no. 3, 2017.
  - [44] L. M. Grubbs, M. Saifullah, E. Nohelli, S. Ye, S. S. Achi, W. E. Acree Jr, and M. H. Abraham, “Mathematical Correlations for Describing Solute Transfer into Functionalized Alkane Solvents Containing Hydroxyl,

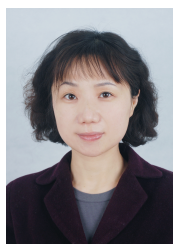
- Ether, Ester or Ketone Solvents,” *Fluid Phase Equilibria*, vol. 298, no. 1, pp. 48–53, 2010.
- [45] F. H. Vermeire and W. H. Green, “Transfer Learning for Solvation Free Energies: From Quantum Chemistry to Experiments,” *Chemical Engineering Journal*, vol. 418, p. 129307, 2021.
- [46] W. Zhang, Y. Chen, F. Liu, F. Luo, G. Tian, and X. Li, “Predicting Potential Drug-Drug Interactions by Integrating Chemical, Biological, Phenotypic and Network Data,” *BMC Bioinformatics*, vol. 18, pp. 1–12, 2017.
- [47] D. S. Himmelstein and S. E. Baranzini, “Heterogeneous Network Edge Prediction: A Data Integration Approach to Prioritize Disease-Associated Genes,” *PLoS Computational Biology*, vol. 11, no. 7, p. e1004259, 2015.
- [48] D. S. Wishart, Y. D. Feunang, A. C. Guo, E. J. Lo, A. Marcu, J. R. Grant, T. Sajed, D. Johnson, C. Li, Z. Sayeeda *et al.*, “DrugBank 5.0: A Major Update to the DrugBank Database for 2018,” *Nucleic Acids Research*, vol. 46, no. D1, pp. D1074–D1082, 2018.
- [49] G. Karypis and V. Kumar, “Multilevel Algorithms for Multi-Constraint Graph Partitioning,” in *Proceedings of the ACM/IEEE Conference on Supercomputing*, 1998, pp. 28–28.
- [50] Y. Pathak, S. Laghuvarapu, S. Mehta, and U. D. Priyakumar, “Chemically Interpretable Graph Interaction Network for Prediction of Pharmacokinetic Properties of Drug-Like Molecules,” in *Proceedings of the 34th AAAI Conference on Artificial Intelligence*, vol. 34, no. 01, 2020, pp. 873–880.
- [51] A. K. Nyamabo, H. Yu, and J.-Y. Shi, “SSI-DDI: Substructure–Substructure Interactions for Drug–Drug Interaction Prediction,” *Briefings in Bioinformatics*, vol. 22, no. 6, p. bbab133, 2021.
- [52] J. A. F. Diniz-Filho, T. N. Soares, J. S. Lima, R. Dobrovolski, V. L. Landeiro, M. P. d. C. Telles, T. F. Rangel, and L. M. Bini, “Mantel Test in Population Genetics,” *Genetics and Molecular Biology*, vol. 36, pp. 475–485, 2013.
- [53] D. Chen, Y. Zhu, J. Zhang, Y. Du, Z. Li, Q. Liu, S. Wu, and L. Wang, “Uncovering Neural Scaling Laws in Molecular Representation Learning,” *Advances in Neural Information Processing Systems*, vol. 36, 2024.
- [54] D. Wu, W. Sun, Y. He, Z. Chen, and X. Luo, “MKG-FENN: A Multimodal Knowledge Graph Fused End-to-End Neural Network for Accurate Drug–Drug Interaction Prediction,” in *Proceedings of the 38th AAAI Conference on Artificial Intelligence*, vol. 38, no. 9, 2024, pp. 10 216–10 224.
- [55] Y. Wang, Y. Xiong, X. Wu, X. Sun, J. Zhang, and G. Zheng, “DDIPrompt: Drug-Drug Interaction Event Prediction based on Graph Prompt Learning,” in *Proceedings of the 33rd ACM International Conference on Information and Knowledge Management*, ser. CIKM ’24. New York, NY, USA: Association for Computing Machinery, 2024, p. 2431–2441.
- [56] H. Xiang, L. Zeng, L. Hou, K. Li, Z. Fu, Y. Qiu, R. Nussinov, J. Hu, M. Rosen-Zvi, X. Zeng *et al.*, “A Molecular Video-Derived Foundation Model for Scientific Drug Discovery,” *Nature Communications*, vol. 15, no. 1, p. 9696, 2024.
- [57] Y. Zhong, G. Li, J. Yang, H. Zheng, Y. Yu, J. Zhang, H. Luo, B. Wang, and Z. Weng, “Learning Motif-Based Graphs for Drug–Drug Interaction Prediction via Local–Global Self-Attention,” *Nature Machine Intelligence*, vol. 6, no. 9, pp. 1094–1105, 2024.
- [58] R. Zhang, X. Wang, P. Wang, Z. Meng, W. Cui, and Y. Zhou, “HTCL-DDI: A Hierarchical Triple-view Contrastive Learning Framework for Drug–Drug Interaction Prediction,” *Briefings in Bioinformatics*, vol. 24, no. 6, p. bbad324, 09 2023.
- [59] C. Zhou, P. Liu, P. Xu, S. Iyer, J. Sun, Y. Mao, X. Ma, A. Efrat, P. Yu, L. Yu *et al.*, “Lima: Less is More for Alignment,” *Advances in Neural Information Processing Systems*, vol. 36, 2024.
- [60] A. Köpf, Y. Kilcher, D. von Rütte, S. Anagnostidis, Z. R. Tam, K. Stevens, A. Barhoum, D. Nguyen, O. Stanley, R. Nagyi *et al.*, “Openassistant Conversations-Democratizing Large Language Model Alignment,” *Advances in Neural Information Processing Systems*, vol. 36, 2024.
- [61] J. Ji, M. Liu, J. Dai, X. Pan, C. Zhang, C. Bian, B. Chen, R. Sun, Y. Wang, and Y. Yang, “Beavertails: Towards Improved Safety Alignment of LLM via a Human-Preference Dataset,” *Advances in Neural Information Processing Systems*, vol. 36, 2024.
- [62] H. R. Kirk, B. Vidgen, P. Röttger, and S. A. Hale, “The Benefits, Risks and Bounds of Personalizing the Alignment of Large Language Models to Individuals,” *Nature Machine Intelligence*, pp. 1–10, 2024.
- [63] T. Hamamsy, J. T. Morton, R. Blackwell, D. Berenberg, N. Carriero, V. Gligorijevic, C. E. Strauss, J. K. Leman, K. Cho, and R. Bonneau, “Protein Remote Homology Detection and Structural Alignment Using

Deep Learning,” *Nature Biotechnology*, vol. 42, no. 6, pp. 975–985, 2024.

- [64] Y. Wang, D. Wang, H. Liu, B. Hu, Y. Yan, Q. Zhang, and Z. Zhang, “Optimizing Long-tailed Link Prediction in Graph Neural Networks through Structure Representation Enhancement,” in *Proceedings of the 30th ACM SIGKDD Conference on Knowledge Discovery and Data Mining*, 2024, pp. 3222–3232.
- [65] J. Mu, Z. Li, B. Zhang, Q. Zhang, J. Iqbal, A. Wadood, T. Wei, Y. Feng, and H.-F. Chen, “Graphormer Supervised De Novo Protein Design Method and Function Validation,” *Briefings in Bioinformatics*, vol. 25, no. 3, p. bbae135, 2024.
- [66] X. Jiang, L. Tan, and Q. Zou, “DGCL: Dual-Graph Neural Networks Contrastive Learning for Molecular Property Prediction,” *Briefings in Bioinformatics*, vol. 25, no. 6, p. bbae474, 2024.



**Peiliang Zhang** (Student Member, IEEE) is pursuing his Ph.D. degree at Wuhan University of Technology, Wuhan, China. He is also currently a visiting Ph.D. student at Yonsei University, Republic of Korea. Before that, in 2022, he received his M.S. degree in software engineering from Dalian University, Dalian, China. His research interests include AI for Science, Molecular Representation and Medical Informatics.



**Jingling Yuan** (Senior Member, IEEE) received the Ph.D. degree from the Wuhan University of Technology, China, in 2004. She is currently a Professor with the School of Computer Science and Artificial Intelligence, Wuhan University of Technology. She was a Visiting Scholar with the University of Florida from 2008 to 2009, and a Research Scholar with the University of Bristol in 2018. Her research interests include Machine Learning, Green Computing and AI for Science.

She has published 80+ publications such as AAAI, ACM MM, ECCV, WSDM, DASFAA, IEEE TMM, ACM TKDD and so on.



**Qing Xie** is currently an Associate Professor in School of Computer Science and Artificial Intelligence at Wuhan University of Technology. He received the BE degree in information science from University of Science and Technology of China in 2008, and the Ph.D. degree in computer science from the University of Queensland in 2013. After that, he worked as a postdoctoral research fellow at King Abdullah University of Science and Technology. His research interests include Multimedia Analysis, Recommender System and Knowledge Engineering.



**Yongjun Zhu** received his Ph.D. from Drexel University and he is currently an Associate Professor of the Department of Library and Information Science at Yonsei University, Republic of Korea. He researchers broadly Science of Science, Mental Health Informatics, and Philosophical and Societal Aspects of Artificial Intelligence.



**Lin Li** (Senior Member, IEEE) received her Ph.D. from The University of Tokyo, Japan in 2009. She is currently a Professor at the School of Computer Science and Artificial Intelligence, Wuhan University of Technology, China. Her research interests cover Cnformation Retrieval, Recommender System, and Multimodal Machine Learning.

She has published 100+ publications such as IJ-CAI, AAAI, WWW, ICDM, SIGIR, ICMR, CIKM, DASFAA, ACM TOIS, ACM TOIT, ACM TIST, IEEE TSC, IEEE TKDE, IEEE TCSS and so on.